Assessing the Impact of Gold Mining on Forest Cover in the Surinamese Amazon Rainforest

from 1997 – 2019: A Semi-Automated Satellite Based Approach

Yann Quash

A Thesis

in

The Department

of

Geography, Planning and Environment

Presented in Partial Fulfillment of the Requirements

for the Degree of Master of Science (Geography, Urban and Environmental Studies) at

Concordia University

Montreal, Quebec, Canada

February 2023

CONCORDIA UNIVERSITY

School of Graduate Studies

This is to certify that the thesis prepared

By: Yann Quash

Entitled: Assessing the Impact of Gold Mining on Forest Cover in the Surinamese
                       Amazon Rainforest from 1997 – 2019: A Semi-Automated Satellite Based
                       Approach

and submitted in partial fulfillment of the requirements for the degree of:

Master of Science (Geography, Urban and Environmental Studies)

complies with the regulations of the University and meets the accepted standards with respect to
originality and quality.

Signed by the final Examining Committee:

Chair: Dr. Jochen Jaeger

Examiner: Dr. Jochen Jaeger

Examiner: Dr. Heather McNairn

Thesis Supervisor: Dr. Angela Kross

Approved by: Dr. Damon Matthews

        Graduate Program Director

Approved by: Dr. Pascale Sicotte

        Dean of Faculty of Arts and Science

ABSTRACT

Assessing the Impact of Gold Mining on Forest Cover in the Surinamese Amazon Rainforest from 1997 – 2019: A Semi-Automated Satellite Based Approach.

Yann Quash

The Amazon rainforest, as a biodiversity hotspot and regulator of the earths climate, is one of the most important ecosystems on earth, but has been facing extensive deforestation for decades due to urban growth, agricultural expansion, logging and mining. Mining (and the use of remote sensing methods to detect it) has been relatively understudied in the Amazon compared to the other drivers up until a decade ago, highlighting the importance of current research. The objectives of this study are: To quantify the increase in industrial and artisanal mining and its impact on forest cover in the northern Amazonian country of Suriname between 1997 and 2019; Evaluate the impact of this expansion on the structure (fragmentation) and health (phenology) of the forest; and improve existing remote sensing techniques for mining detection through the development of a pioneer method based on cloud processing and semi-automated mining reclassification. The cloud processing software known as Google Earth Engine (GEE) was used for the initial land use land cover classification of the study area. Landsat 5 and 8 images and the classification and regression trees (C.A.R.T) algorithm were used in this step. The resulting classified maps were fed into the semi-automated re-classification model developed for this study, producing final re-classified output maps, which were used to analyse the expansion of mining and its associated impacts on forest fragmentation and phenology. The proposed method is the first documented method which combines cloud processing with a semi-automated re-classification model, providing a technologically advanced approach capable of rapid and efficient detection of mines. This approach resulted in an 89.5% accuracy of mining detection, and the combination of speed, efficiency, and highly accurate detection outperformed many of the other currently documented methods for mining detection in the Amazon. The results highlighted that mining increased from 69.4km² in 1997 to 431.6km² in 2019, an increase of 522% over 22 years. This growth led directly to 351.9km² of forest loss, 83% of which was due to artisanal mining. This loss of forest led to a 122.8km² reduction in the effective mesh size for the artisanal mine

sub-area, compared to a decrease of 83km² for the Industrial mine sub-area. Mining also caused a decrease in the health of the surrounding forest, with the decrease in peak greenness being more pronounced for artisanal mining compared to industrial mining. Recommendations for future research include exploring the use of higher resolution imagery such as Sentinel for better results, as well as the use of microwave data in the classification to combat the issue of extensive cloud cover in the Amazon. The issue of overclassification present in the proposed method can potentially be combated by exploring combinations of different classification algorithms with the reclassification model.

ACKNOWLEDGMENTS

In order for this research project to have been completed successfully, I'd like to first and foremost give the utmost thanks to my supervisor, Dr. Angela Kross, for her unwavering support, guidance and understanding throughout all stages of the research process. The completion of this thesis would not have been possible without her. I'd also like to thank Dr. Jochen Jaeger for his expert advice with the fragmentation section of my research, Dr. Heather McNairn for her insightful comments during my thesis defence, and Dr. Jeannine St. Jacques for her feedback during the thesis proposal process. Lastly, I'd also like to thank Mrs. Jennifer Srey, who's coordination and support during the most challenging of times brought about by the COVID 19 pandemic ensured that the process of completing an MSc during the pandemic was as smooth a process as possible.

CONTENTS

LIST OF FIGURES

LIST OF TABLES

LIST OF ACRONYMS

List of important and recurring acronyms used in the paper:

LULC - Land use / land cover

ASGM - Artisanal and small-scale gold mining

GEE - Google Earth Engine

CART - Classification and Regression Trees

MODIS - Moderate Resolution Imaging Spectroradiometer

EVI - Enhanced Vegetation Index

1. INTRODUCTION

The Amazon rainforest is one of the most biodiverse regions on earth and plays a key role in ecological and climatic processes on both local and global scales (Sanchez-Cuervo et al.. 2020). However, over the last few decades, large areas of the Amazon have been cleared due to various drivers such as state-driven urban growth and highway construction (Hargrave and Kis-Katos 2013), logging (Asner 2005) and agricultural expansion (Fehlenberg et al.. 2017). Mining, both industrial and artisanal, is another major driver of land cover change in the Amazon that leads to detrimental impacts on forest cover and biodiversity. Early research however focused almost exclusively on the impacts of land cover change due to agricultural expansion, with the monitoring of the land cover changes due to mining having been given relatively little attention (Almeida-Filho 2002). It is only within the last decade that research began to focus on the use of remote sensing methods to map and analyse the growth of mining areas and its impact on forest cover. Research on this topic began with early papers by Peterson and Heemskerk (2001) and Almeida-Filho (2002), but only gained prominence as of 2013 when research began to focus in more detail on land cover change due to mining (Asner 2013; Elmes et al. 2014; Asner and Tupayachi 2016; Sonter et al. 2017; Caballero-Espero et al. 2018; Lobo et al. 2018; Nicolau et al. 2019).

Most previous studies have focused on the western and southern parts of the Amazon, while the northern Amazon has been largely ignored. The only studies on this area were by Peterson and Heemskerk (2001), and Rahm (2015). This research will therefore focus on the northern Amazonian country of Suriname, which is plagued by a plethora of gold mining operations at a variety of scales. While a very small area of Bauxite mining is present near the capital city, gold mining is currently the major mining activity which dominates the landscape in Suriname. According to Kioe-A-Sen et al. (2016), since the 1800s, gold has always been a major economic asset in Suriname and was extracted primarily by small scale artisanal mines concentrated in the greenstone belt in the northeast of the country. More recently, there has been an increasing development of large-scale industrial gold mines such as the Rosabel and Merian mines. The Rosebel mine (initially operated by Canadian company Iam Gold, recently sold to Chinese company Zijin Mining), has been in operation since 2000 and as of 2013, was responsible for 46% of Suriname's entire gold production, while the Merian mine first began production in 2016 and is owned and operated by the American company Newmont Mining. The development of these industrial mines since 2000, in combination with the relative lack of existing studies in the area makes research in this region even more pressing and important.

In Suriname, while industrial gold mining is prominent, there is another major mining type of gold mining known as artisanal and small-scale gold mining, or ASGM, which since 1998, has been growing in the Amazon region at an alarming rate (Caballero Espejo et al. 2018). Industrial mining refers to mining conducted on a large scale, where mines are owned and operated by multinational companies with deep ties to both the global financial and international mineral markets (Kemp and Owen 2019). ASGM on the other hand, can be defined as "mining by individuals, groups or co-operatives with minimal or no mechanisation, often in the informal sector of the market" (Hentschel et al. 2002). The majority of ASGM mining production in Suriname uses modern machinery and hydraulicking (process through which water is used to loosen and fracture the soil to remove the top layers of sand and clay) and focuses on alluvial gold deposits. These ASGM sites flourish along rivers in the Amazon forest and cause enormous environmental impacts including the alteration of river morphology, deforestation, biodiversity and landscape degradation, and widespread environmental pollution (Castello and Macedo 2016).

While these issues make the need for current research critical, this need will become even more crucial in the future as mining activities in the Amazon are expected to expand in the near future. According to Galbraith and Kalamandeen (2020), the current economic crisis caused by the COVID 19 pandemic is expected to drive gold prices up (they have already increased by 25% in 2020 compared to 2019), due to the role of gold as a perceived economic stabilizer. This will likely incentivize both small scale and industrial mining activities to expand, justifying the continued need for research on the impacts of mining on forest cover and the environment.

The goal of this study is therefore to add to the existing body of work on the impacts of mining on forests and raise awareness on an issue that has often been overlooked in the face of other causes of deforestation in the Amazon. This study aims to develop a new remote sensing approach to improve the detection and mapping of mines, to analyse how mining has progressed over the last two decades and how this has in turn impacted forest quantity and quality.

2. LITERATURE REVIEW

To understand the context and significance of this research, this literature review compiles peer reviewed articles from established scientific databases such as Web of Science, seeking to answer the 4 review questions of: Why is the Amazon rainforest important? What are the drivers of land cover change in the Amazon? How has mining impacted forest cover? What are the remote sensing methods used to study the impacts of mining on forest cover quantity and quality? In order to answer these questions, the following topics will be discussed (Figure 1).

IMPACT OF MINING ON FOREST COVER IN THE SURINAME AMAZON RAINFOREST

IMPORTANCE OF THE AMAZON

Carbon Sink
Park (2002) ; Barbosa (2000) ; Soares-Filho et al (2010) ; Ahlstrom et al (2012)

Regulator of Energy Fluxes
Manoli et al (2018) ; Pinage et al (2020) ; Girardin et al (2016) ; Kim et al (2012)

Biodiversity Hotspot
Lopez-Quintero et al (2012) ; Cardoso et al (2017) ; Rodrigues (2006) ; Albert et al (2011) ;

DRIVERS OF LAND COVER CHANGE IN THE AMAZON

Urban Growth
Boucher and Chi (2018) ; Boucher et al (2013) ; Hargrave and Kis-Katos (2013)

Agricultural Expansion
Barona et al (2010) ; Fehlenberg et al (2017)

Logging
Asner (2005) ; Le Tourneau (2016)

Mining
Heemskerk (2002) ; Asner et al (2013) ; Sonter et al (2013)

IMPACT OF MINING ACTIVITIES ON FORESTS

Impact of mining on forest cover quantity and composition
Asner and Tupayachi (2016) ; Swenson et al (2011) ; Sonter et al (2017) ; Peterson and Heemskerk (2001)

Impact of mining on forest structure (Fragmentation)
Batar et al (2017) ; T.V et al (2016) ; Siquiera-Gay et al (2020) ; tagiewicz (2014) ; Malaviya et al (2010) ; Kumi et al (2021)

Ecological Impacts
Velasquez Ramirez et al (2020) ; Malm (1998) ; Hacon et al (2020) ; Pinheiro et al (2007)

REMOTE SENSING METHODS FOR MEASURING IMPACT OF MINING ON FORESTS

Measuring forest cover quantity: Classification
Almeida-Filho (2002) ; Charou et al (2010) ; Asner et al (2013) ; Elmes et al (2014) ; Asner and Tupayachi (2016) ; Caballero Espejo et al (2018) ; Nicolau et al (2019) ; Lobo et al (2018)

Measuring forest cover quality: Fragmentation
Riitters et al (2000) ; Moreno-Sanchez (2009) ; Chakraborty et al (2017) ; TV et al (2016) ; Clay et al (2016) ; Wulder et al (2011) ; Girvertz et al (2008) ; Jaeger et al (2007) ; Jaeger et al (2008) ; Roch and Jaeger (2014)

Measuring forest cover quality: Phenology
Koltunov et al (2009) ; Pinage et al (2020) ; Moreau and Defourny (2012) ; Ratana et al (2006)
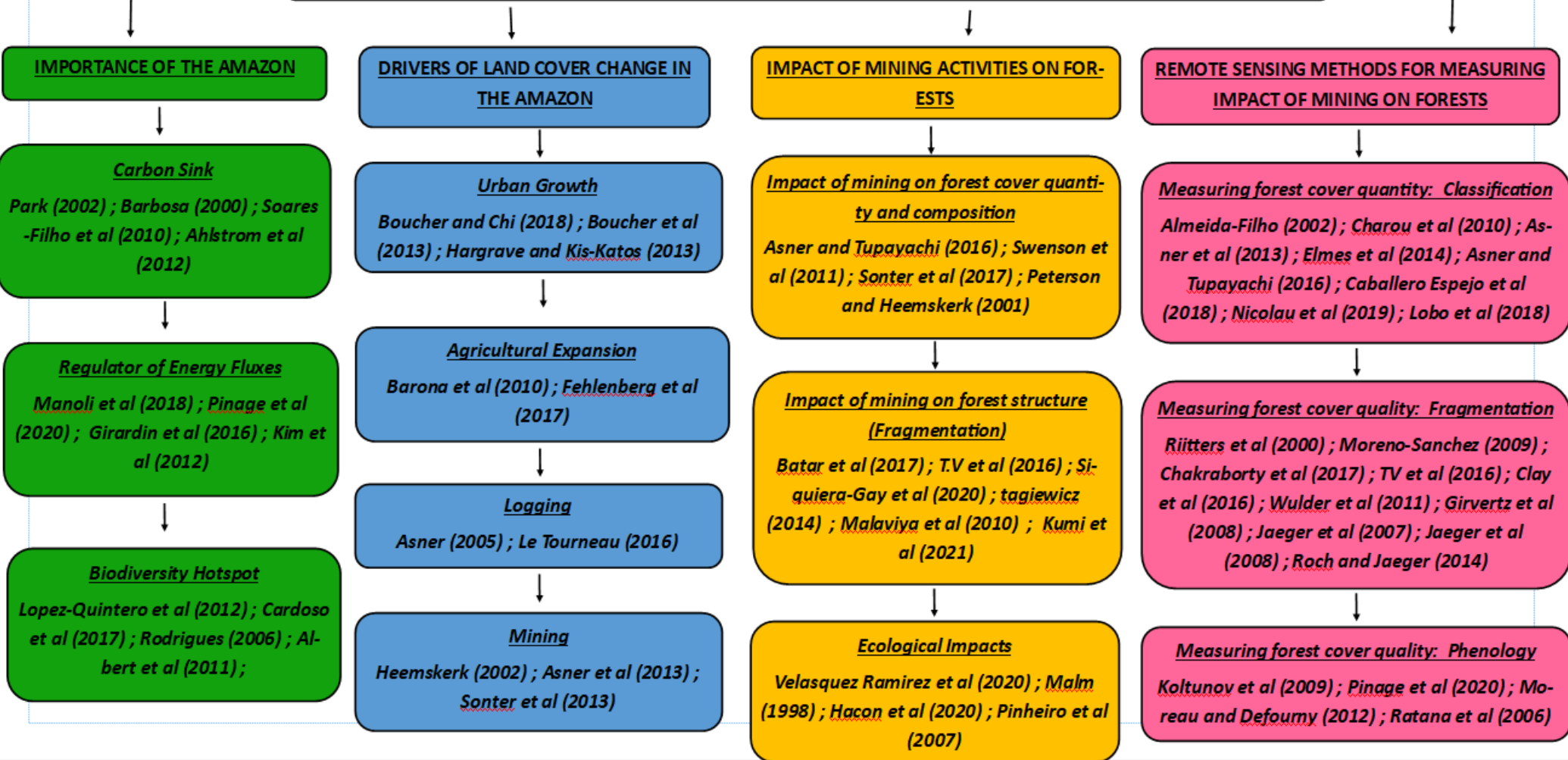
Figure 1: Literature Review map showing the papers used for each topic in the Literature Review

4

2.1 IMPORTANCE OF THE AMAZON

Tropical rainforests, also known as jungles, are among the most complex ecosystems on earth. They are the natural climax vegetation of the tropical zone and are located within 23.5⁰ of the equator, but thrive particularly in the lower latitudes within 10⁰ of the equator. In the tropics, they have been the most dominant form of vegetation for millions of years and boast a diversity of species that is unrivalled anywhere on earth (Park 2002). The Amazon rainforest is a tropical rainforest that spans across the majority of northern South America and is the largest rainforest on the planet. The Amazon rainforest encompasses around 7 million square kilometres, over two thirds of which are located in Brazil, making it the biggest holder of the world's largest remaining tropical rainforest (Barbosa 2000).

The Amazon rainforest, often referred to as the 'lungs of the earth' is the most important tropical rainforest on the planet due to the multitude of benefits it provides to our climate, biodiversity and water supply. Tropical rainforests such as the Amazon play a key part in the world's climate system due to their ability to store large stocks of carbon and regulate carbon, energy and water fluxes (Soares-Filho et al. 2010). Forest's role in the terrestrial carbon cycle can be divided into two major fluxes. The uptake flux, known as net primary production refers to carbon sequestration by plants through the processes of photosynthesis. The opposing flux is the release of carbon to the atmosphere through plant and soil respiration (by microbes that consume dead organic matter). The difference between these two large fluxes is the net land-atmosphere flux, known as the net biome production, which is currently responsible for sequestrating 30% of global anthropogenic emissions (Ahlstrom et al. 2012). The importance of tropical rainforests as a carbon sink therefore cannot be understated. This is reinforced in a study done by Soares Filho et al. (2010), who sought to estimate the role of protected areas (PAs) in the Amazon rainforest in reducing carbon fluxes to the atmosphere. By analysing 595 Brazilian Amazon PAs, they found that the expansion of PAs in Brazil were responsible for 37% of the region's reduction in deforestation between 2004 and 2006. Most importantly, these PAs, if fully implemented, can potentially avoid 8.0 ± 2.8 Pg of carbon emissions by 2050 (Soares-Filho et al. 2010).

The importance of the Amazon as a carbon sink and the subsequent benefits it provides to our climate hinges strongly upon the underlying mechanisms driving monthly changes in carbon fluxes. These mechanisms, known as vegetation phenology, is part of the metabolic rhythm of the Amazon rainforest and is a crucial component of terrestrial biogeochemical cycles (Manoli et al. 2018). Phenology can be defined as a sequence of seasonal changes in leaf development, area, and physiology, which drive

seasonal variations in land-atmospheric fluxes such as photosynthesis and respiration due to the dependence of these fluxes on leaf quality, quantity and other important leaf characteristics (Pinage et al. 2020). The phenological pattern of the Amazon rainforest has been well researched, with the Amazon displaying a surge in leaf production and 'greening' of the forest canopy towards the end of the dry season in October and November (Girardin et al. 2016; Manoli et al. 2018; Pinage et al. 2020). This canopy 'greenness' can be measured using satellite-derived spectral vegetation indices (VIs). The enhanced vegetation index (EVI), for example, is associated with an overall increase in net ecosystem productivity, net primary production (NPP) and evapotranspiration (Kim et al. 2012; Girardin et al. 2016). According to Manoli et al. (2018), while this 'greenup' and associated increased carbon uptake is dependent on hydro-climatic (temperature and precipitation) variations, the role of phenology and leaf mechanisms is crucial and cannot be understated. Their study used camera observations and leaf measurements to show that at the end of the dry season there is a "synchronization between dry season litterfall and the subsequent onset of new, greener leaves which have a higher photosynthetic capacity and light use efficiency" (Manoli et al. 2018, pg. 1910). This is corroborated by Girardin et al. (2016), who added that this onset of new leaves or 'leaf flush' at the end of the dry season and the associated change in photosynthetic capacity is the main driver of the greenup cycle and increased carbon uptake at this time of year in the Amazon rainforest.

In addition to its importance as a carbon sink and regulator of energy fluxes, the Amazon is also important for the wide array of biodiversity it supports. According to Lopez-Quintero et al. (2012, pg. 2222), "The Amazon Rainforest is arguably the most species rich terrestrial ecosystem in the world". In fact, the Amazon Rainforest is believed to host more than 50% of the worlds plant and animal species, the majority of which are still uncatalogued (Barbosa 2000). The exact number of plant species in the Amazon is a long standing question that to this date remains unresolved, with some studies estimating that the region holds up to 50,000 plant species (Cardoso et al. 2017), while others place this number slightly higher at 60 000 plant species (Lopez-Quintero et al. 2012). Of this large number of plant species, it is estimated that 25000 to 30000 are endemic species (Rodrigues 2006). The Amazon is home to a vast number of large tree species, with an estimated 48% of all tree species in the Amazon reaching a stem diameter of >10 cm at breast height. Of the seed plant species in the Amazon, 52% is comprised of shrubs, small trees, vines and herbs, with the Leguminosae family being the most species rich (Cardoso et al. 2017). According to Albert et al. (2011), the aquatic biodiversity of the region is equally impressive, as the Amazon is home to more than 5,600 species, which includes the majority of the worlds freshwater fishes. In fact, over 10% of all known vertebrate species on earth are estimated to reside in the Amazon, which

is even more remarkable when considering the fact that the Amazon waters make up less than 0.002% of the earth's total liquid water supply (Albert at al 2011).

2.2 DRIVERS OF LAND COVER CHANGE IN THE AMAZON

Despite its importance to the climate system and terrestrial and aquatic biodiversity, the Amazon has undergone a lot of changes over the last few decades as swathes of its forest cover have been lost. According to Barbosa (2000), deforestation in the Amazon began to accelerate starting in the mid-1970s, where 152 200 km² of forest had been cleared, which increased to a rate of 225 000 km² per decade during the 1980s. Boucher and Chi (2018) add that these very high deforestation rates continued at the end of the 20th and beginning of the 21st century, where the Amazon rainforest lost approx. 19,500 km² per year between 1996 and 2005. After 2005, this high rate of deforestation began to decline, with the levels of deforestation having been reduced by over two thirds of what it was in the previous decade of 1996-2005 (Boucher et al. 2013).

This deforestation of the Amazon that has occurred over the last few decades can be attributed to many underlying driving forces. The first major driver of deforestation is urban growth. According to Hargrave and Kis-Katos (2013), deforestation of the Brazilian Amazon began in the 1960's as a result of state driven infrastructure and settlement projects, such as the rural settlements policy (executed by the National Agency for Land Reform), and the construction of national highways that cut through the Amazon rainforest. These combined at the time (1960s) to incite yearly deforestation at a rate of about 10,000 km² per year (Hargrave and Kis-Katos 2013)

Another important driver of land cover change in the Amazon is agricultural expansion. According to Barona et al. (2010), the major driving force behind land cover change in the Amazon has been agricultural land use change. Due to rising commodity prices, the availability of cheap labour, and the favourable climatic conditions, South America has become a frontier for agricultural expansion into forested areas, especially with regards to soybean and beef production (Fehlenberg et al. 2017). Today, these factors have made Brazil one of the worlds largest exporters of agricultural products, especially soybean, which has been the most harvested crop in the Brazilian Amazon in terms of area since 1990 (Barona et al. 2010). Cattle ranching for beef production, which was marginalised until 1970, has grown

by over 840% from 1974 to 2015, and is also responsible for the encroachment into the Amazon (Le Tourneau 2016). This encroachment into the Amazon is especially prominent in the southern edge of the forest known as the arc of deforestation. This agricultural expansion has led to 189 000 km² of land to have been deforested in the Brazilian Amazon between 2000 and 2006 (Barona et al. 2010).

Land cover change in the Amazon is also due to logging, which involves to the removal of forested areas for the acquisition of timber. This issue of logging in the Amazon has been driven by land speculation, which is the mechanism whereby the intact rainforest is considered more of a liability than an asset, and landowners make noteable profits by deforesting their lands and selling the timber (Le Tourneau 2016). In a study conducted by Asner (2005), high resolution, automated remote sensing analysis was done on selective logging in the Brazilan Amazon. The study found that between 1992 and 2002, logging was responsible for 12 075 to 19 823 km² of forest removal per year, while every year, between 27 and 50 million cubic meters of wood were extracted.

Mining is another major driver of deforestation, which has seen an unprecedented rise in the larger Amazon region since the 1970s gold rush in Brazil (Heemskerk 2002). Despite an increase in mining in the region since this time, where gold rushes have come and gone, the real upsurge in mining activity came in 2008, as the global financial crisis caused a substantial increase in commodity gold prices, which fuelled the demand for gold (Asner et al. 2013). In the Brazilian Amazon, mining exploration permits, leases and concessions cover over 1.65 million km² of land, with approx. 60% of this area being located in the Amazon rainforest. Mining in Brazil was directly responsible for 11,670 km² of forest loss between 2005 and 2015, which represents 9% of all forest loss in the Amazon in that time period (Sonter et al. 2017).

This increase in the extent and severity of mining activities was consistent in other Amazonian regions, such as Peru, where gold mining increased by 400% between 1999 and 2012, and the rate of deforestation due to mining tripled following the 2008 global recession and gold price surge (Asner et al. 2013). The increase in mining in the Amazon has not just been pushed forward by large mining corporations, but there has also been a huge surge in small scale mining by independent small-scale entrepreneurs. This is often welcomed by Amazon countries as it provides income for the poorest population, albeit at the expense of rampant forest degradation and other environmental impacts (Heemskerk 2002).

2.3 IMPACT OF MINING ACTIVITIES ON FORESTS

Mining in the Amazon is a major concern, as it has an impact on forest cover and by extension its structure and composition. According to Asner and Tupayachi (2016), in a study of the impact of mining in the Peruvian Amazon, found that mining causes not just widespread and extensive deforestation, but also leads to progressive forest loss over time. In Peru, mining related losses varied from a minimum rate of 10 km² per year in 1999-2000, to a maximum of rate of 80 km² per year between 2013-2014, and importantly, as of 2016, 5.2 km² of forest have been lost even in protected/forest reserve areas (Asner and Tupayachi 2016). In another study on mining-induced forest loss in Peru conducted by Swenson et al. (2011), found that between 2003-2009, 66 km² of wetlands and primary tropical forests was converted into mines. Their impact in environmental and ecological terms far overshadows that of settlement deforestation. Sonter et al. (2017) added that the impact of mining on forest cover is not just confined to within the boundaries of the mining concessions, but also leads to extensive off-lease impacts up to 70km from mining leases. This occurs through secondary pathways such as "mining infrastructure establishment and associated secondary forest clearing such as establishment of new roads" (Sonter et al. 2017).

This removal of this forest cover caused by mining subsequently also impacts forest composition. A study conducted on the impacts of small-scale gold mining in Suriname by Peterson and Heemskerk (2001) found that the forest cover and composition of mined sites differed greatly from untouched, old-growth forest. While old-growth forests were characterised by dense, healthy forest cover and an abundance of leaf litter, abandoned mined sites were dominated by large areas of exposed bare rock and sand, grass, vines, and large pools of stagnant, open water. None of these land cover types were prevalent in old-growth forests, and the study also found that regeneration of forests on mined sites was very slow (Peterson and Heemskerk 2001).

In addition to its impacts on forest composition, mining and its associated loss of forest cover also impacts forest structure through the alteration and fragmentation of the forested landscape. According to Batar et al. (2017), forest cover loss and fragmentation, while closely related, also share an important distinction. Forest loss refers to the conversion of forested land into another form of land use such as agriculture or urban areas, whereas forest fragmentation refers to the particularly distinct phenomenon whereby a large patch of forest is broken up into a collection of smaller patches which are physically disconnected from each other (Batar et al. 2017). This fragmentation results in a phenomenon whereby the landscape

resembles a mosaic of natural patches which are bordered by other land uses and can lead to detrimental effects on bio-geo chemical, nutrient and water cycling within a forest ecosystem (T.V et al. 2016).

Mining is one such driver of land use change which leads to fragmentation, and in a study about mining in the east Amazonian region of Renca, Siqueira-Gay et al. (2020), found that mining not only caused forest loss, but also led to the fragmentation of forests due to the infrastructure such as roads/railways, etc that are required to process and transport the extracted materials. This fragmentation has notable effects on landscape patterns and structure and leads to "a higher number of patches, decreased average size of patches, increased edge effects and increased nearest neighbour distance" (Siqueira-Gay et al. 2020).

According to Fagiewicz (2014) mining activities result in a progressive process of fragmentation which leads to irreversible and permanent changes to the landscape. In their study conducted on opencast lignite mines in Poland, they found that the post-mining landscape was more complex with a greater variety of land uses resulting from anthropogenic pressure. The mining activities also resulted in an increase in the number of patches of forest from 161 to 347, a decrease in the average area of each patch from 0.1 km² to 0.067 km², and an increase in the length of the edges of forests, which almost doubled from 113.52 km to 209.42 km (Fagiewics 2014).

These statistics are very useful indicators of fragmentation at the landscape level, and are often used to determine the presence and extent of fragmentation in a post-mining landscape. In a study assessing and quantifying the impacts that mining had on LULC change and fragmentation in Central India, Malaviya et al. (2010) found that the number of patches increased from 243 in 1972 to almost double that number in 421 in 2006, which indicates considerable fragmentation.

Mining activities and the resulting fragmentation of forests also pose a threat to plant species diversity, especially in tropical forests. The separation and isolation of patches of forest from each other in a fragmented landscape makes movement of native species from one patch to another much more difficult. This, combined with the edge effects which place harsh constraints on plant species near the edge of fragments leads to elevated levels of species mortality and the subsequent reduction of plant species diversity (Kumi et al. 2021).

Mining not only impacts forest structure and composition but also leads to severe and persistent ecological impacts both on and off-site, as mining strips the forest and soil surface bare (Asner and Tupayachi 2016), leading to serious ecological impacts such as the leaching of heavy metals from mining

sites into waterways (Velasquez-Ramirez et al. 2020) and the subsequent contamination of fish species, especially predator species higher up the trophic levels (Malm 1998). This contamination of fish species poses a great risk to Amazonian communities, indigenous people and riverside communities located downstream of mining sites, as their high consumption of fish is a crucial source of dietary exposure to mercury (Hacon et al. 2020). This risk was researched by Pinheiro et al. (2007) who's study on children's exposure to mercury contamination in Amazonian communities found that hair samples from children (especially those aged two to six) in communities located near to gold mining sites contained higher levels of mercury than samples from communities not affected by gold mining.

2.4 REMOTE SENSING METHODS FOR MEASURING THE IMPACTS OF MINING ON FOREST COVER QUANTITY (DEFORESTATION) AND QUALITY (FRAGMENTATION AND PHENOLOGY)

2.4.1 MEASURING FOREST COVER QUANTITY: LAND USE LAND COVER (LULC) CHANGE AND DEFORESTATION

Land cover classification can be used to quantify deforestation over time and space and allows for the identification of key drivers of forest cover change. Remotely sensed images can be used to classify mining areas and their changes over time. According to Almeida-Filho (2002), there are two main methods for conducting change detection studies in mining regions. The first is image enhancement, which is the transformation of images into a combination of new bands that highlights changed areas, while the second, and much more widely used method, the post-classification comparison method, involves the classification of individual images over time, and the subsequent comparison of these images to determine land cover changes. In their study, Almeida-Filho opted for the latter, using 6 different Landsat-5 TM images ranging from March 1987 – February 1999, upon which he conducted image segmentation and region classification, using an unsupervised, K-means clustering algorithm (Almeida-Filho 2002). Charou et al. (2010) were among the few who opted for image enhancement, deciding on a combination of this and classification to assess mining activities. Using both Landsat 5 and 7 images, image enhancement was done through colour-composites and intensity hue saturation images. Unsupervised classification using Artificial Neural Networks (ANNs) was then applied in order to discriminate between land cover classes.

Almeida-Filho (2002) was one of the first to utilize remote sensing techniques for mining detection in the Amazon, and while their early research ushered in the era of using LULC classification techniques for mining detection in the Amazon, it is only a decade later, in 2013, that the use of LULC classification really began to gain traction in mining studies, and more refined and sophisticated techniques began to be used. The research by Asner et al. (2013) began this new age of remote sensing studies on mining in the Amazon. They pioneered the use of spectral unmixing algorithms using the Carnegie Landsat Analysis System Lite (CLASLite) for mining detection. In Peru, they used this method to 'unmix' individual Landsat 5 and 7 pixels into subpixel fractional land cover values of photosynthetic vegetation, non-photosynthetic vegetation, and bare substrate. Mines were then determined as pixels with at least 25% bare substrate. This method was subsequently used by Elmes et al. (2014) in Peru. They also used

a spectral mixture analysis/spectral unmixing of Landsat 5 imagery, followed by a classification tree analysis (CTA) to split the image into 5 final land cover classes; Mining areas, water, agriculture, forest and natural alluvial deposits. This was followed by further research in Peru by Asner and Tupayachi (2016) who also used the spectral unmixing approach in CLASLITE in order to detect gold mining activities.

Caballero Espejo et al. (2018) also used the spectral unmixing / CLASLITE approach but built upon and modified the original unmixing method (Asner et al. 2013). Using their modified approach in the same region of the Peruvian Amazon, they found that using just the CLASLITE approach from previous studies resulted in an underestimation of the total mining area by 30%. Additionally, this old approach failed to identify large water bodies within mines as part of the mine, relying on manual reclassification to reassign these areas (Caballero Espejo et al. 2018). In order to address these shortcomings of under classification, Caballero Espejo et al. (2018) added a post-classification step with the goal of identifying and re-classifying mining areas that were missed when using the initial CLASLITE / spectral unmixing classification from previous studies. Their post-classification step included fusing the initial classified map with the global forest change (GFC) dataset to automatically identify all deforested pixels from the GFC dataset that were within 200 meters of mines in the classified map and assign these deforested pixels to the mining class. For their study, they used 68 landsat TM images spanning 34 years (1985-2017).

Nicolau et al. (2019) used Landsat 7 ETM+ and 8 OLI images from 2013-2018, and like the previous studies by Asner et al. (2013), Elmes et al. (2014) Asner and Tupayachi (2016) and Caballero Espejo et al. (2018), they used the spectral unmixing model in the CLASlite program, where each pixel was separated into sub-classes of photosynthetic vegetation, non-photosynthetic vegetation, and bare substrate. This was followed by change detection, where a deforested pixel was one where the decrease in photosynthetic vegetation fraction between a pre and post image was greater than 50%.

Lobo et al. (2018) diverted from the well-established line of CLASLITE methodologies and used the classification and regression trees (CART) algorithm in Google Earth Engine (GEE) for mining detection in Brazil. They used higher resolution Sentinel-2A images to map mining across 13 regions in Brazil. As the first documented study to utilize cloud processing for mining studies in the Amazon, this method made use of the recent technological advancements to further improve methods of mining detection in the region. However, while the use of cloud processing in this method sped up the process of the initial classification, Lobo et al. (2018) still relied upon extensive manual reclassification of misclassified pixels

in mining regions post-classification, ultimately falling short of the more rapid, *automated* post-classification approach developed by Caballero Espejo et al. (2018).

Following classification map validation in these studies was generally conducted using either high resolution imagery (Planet, Worldview, RapidEye) or Landsat imagery where high resolution data wasn't available. Validation was conducted in order to determine the accuracy of the classified maps. For validation of a classified map, while in-situ collection of validation points through field visits remains the most accurate form of collecting validation points, the use of this method in the literature was limited due to constraints regarding the accessibility of remote forested areas in the Amazon. As the only study that used in-situ collection of validation points, Asner et al. (2013) collected 166 points in the form of field visits in Peru using a handheld GPS system. However, citing the challenges regarding access of other sites due to vegetation conditions, they collected the remaining 1500 validation points from airborne imagery. Elmes et al. (2014) also relied on remote collection of validation points, stating that due to logistical complications of in-situ monitoring, the use of 2.5m Quickbird and Worldview satellite images proved to be a suitable alternative. Using these high-resolution images, they collected 580 validation points (50 points minimum per land cover class) using a spatially stratified sampling design where the points were randomly generated within the study region. Rahm et al. (2015) used high resolution SPOT images from Google Earth to collect validation points, and where imagery wasn't available, validation points were collected using the same satellite imagery for the initial classification. Overall, they collected 8000 validation points using a random sampling approach. Lobo et al (2018) conducted validation using RapidEye classified maps, which were compared to the original classified maps in order to determine the accuracy of the original classification.

2.4.2 MEASURING FOREST COVER QUALITY: FRAGMENTATION AND PHENOLOGY

In order to assess the impact that mining has on forest structure through fragmentation, models which seek to quantify the extent of fragmentation must be employed. Numerous methods have been used over the years to quantify fragmentation, with many being based upon the Riitters et al. (2000) model, which introduced the concept of quantifying fragmentation within fixed area 'windows' of a certain pixel size using the metrics Pf (forest area density) and Pff (forest connectivity). Pf refers to the proportion of the pixels within the window that are forested while Pff refers to the probability that the pixel adjacent to a

forest pixel is also forested. Based on the value of Pf and Pff, the pixel of forest is categorised as either core, perforated, edge or patch (Riitters et al. 2002).

This Riitters model has been heavily used and adapted over the years. In their study on fragmentation of temperate and tropical forests in Mexico, Moreno-Sanchez (2009) opted to follow the Riitters model, using three window sizes of 3*3, 5*5 and 9*9, calculating forest area density (Pf) and forest connectivity (Pff) for the center pixel in each of those windows. Chakraborty et al. (2017), while also basing their model upon the Riitters model, opted to build and expand on it by including two further metrics; anthropogenic fragmentation (Pfa) and natural fragmentation (Pfm). In their analysis of fragmentation in the Uttara Kannada district in India, TV et al. (2016) also opted to use the Riitters model but went further by conducting a post hoc principal component analysis (PCA) to quantify the correlation between the various drivers of forest loss (urban growth, agricultural expansion, population growth, etc.) with the fragmentation of forests.

In addition to the Riitters model, other methods to assess fragmentation include the morphological spatial pattern analysis (MSPA) method adopted by Clay et al. (2016). This method involves the conversion of the forest layers into raster format, and subsequent reclassification into a binary raster in ArcGis which was then imported into the MSPA software. This software, which is used by major conservation and forestry agencies worldwide, "assesses the geometry and connectivity of the input image, as well as user-defined parameters, to determine 7 basic fragmentation classes; Core, Islet, Loop, Bridge, Perforation, Edge and Branch." (Clay et al. 2016). Conversely, Wulder et al. (2011) opted to use the EOSD data and APACK analysis software, and their method focused on using fragmentation metrics that are objective, easy to understand, and widely interpretable across various disciplines. These metrics are the "number of forested patches, proportion of patches that are forested, mean forest patch size, and standard deviation of forest patch size." (Wulder et al. 2011).

While all the metrics listed above and dozens of others have been used to quantify fragmentation, the move towards the consideration of metrics which take into account ecological processes leaves many of these metrics less suitable than other, more developed alternatives (Girvertz et al. 2008). One such metric which also takes into account ecological processes is the effective mesh size. Effective mesh size is based on the probability that two randomly chosen points placed in a landscape will be connected to each other, i.e located in the same patch (Jaeger et al. 2007). According to Roch and Jaeger (2014), "by multiplying this probability by the total area of the reporting unit, it is converted to the size of an area, which is called the effective mesh size." The more barriers present in a landscape is the lower the probability that two

randomly placed points will be connected, and therefore the lower the effective mesh size. A higher effective mesh size means that fewer barriers and less fragmentation are present in the landscape (Jaeger et al. 2008).

The effective mesh size has been widely used as a metric to measure fragmentation. In their study on landscape fragmentation in Switzerland, Jaeger et al. (2008) used the effective mesh size and found it advantageous when compared to other methods as not only was it a single value that was easy to obtain and interpret, but that it was also suitable for comparing fragmentation between regions of different sizes and was confirmed as a reliable method after it was systematically compared to nine other quantitative methods. Girvertz et al. (2008) also used the effective mesh size in their study on landscape fragmentation in California and found that it was the only method that addressed animal dispersal and animal movement processes. In their study on fragmentation in the Canadian Prairies, Roch and Jaeger (2014) also utilized the effective mesh size, noting that it had highly advantageous characteristics when compared to other metrics, as it was not greatly influenced by the inclusion or exclusion of very small patches.

In addition to the general classification and fragmentation methods listed above, the impacts that mining has on forests can also be measured through an assessment of the changes in vegetation phenology of forest areas surrounding mining regions. The remote sensing methods to study phenological changes in the Amazon are well accepted and widely used. According to Koltunov et al. (2009), there are two methods to estimate the phenological impact of a disturbance event: the contextual method and the temporal method. The temporal approach requires a comparison of pre-disturbance and post-disturbance images, while the contextual approach involves measuring the difference between the vegetation index value of a given pixel and that of all of the non-clouded pixels of the same vegetation type within a defined radius of that pixel. Due to a lack of images before the disturbance date, Koltunov et al. (2009) opted for the contextual method, using MODIS NBAR images to calculate the enhanced vegetation index (EVI) and normalized difference water index (NDWI) of a deforested site in the Brazilian Amazon. Pinage et al. (2020) opted to use the temporal method, where they analysed pre and post disturbance images of four 'disturbance sites' of once-burned forest, twice burnt forest, logged forest and intact forest (as a control) in the Amazon. The sites were chosen so that the year of the disturbance event across all 4 sites was the same. For each study site, they derived the enhanced vegetation index (EVI) and normalized burn ratio (NBR) from 288 MODIS 16-day images at a 250m resolution spanning a 12 year period (2002 – 2014). Subsequently, they filled any missing values using linear interpolation and created a pre and post disturbance time series for each of the four study sites, which was analysed to see the phenological changes that occurred due to each disturbances (Pinage et al. 2020).

In their study on the phenology of the Cerrado ecoregion in Brazil, Ratana et al. (2006), like Pinage et al. (2020) opted to use five years of 16 day MODIS images at a 250m resolution, utilizing the MODIS enhanced vegetation index (EVI) time series data in order to determine seasonal variations in phenological patterns. Moreau and Defourny (2012) used ten day composites of SPOT-vegetation (VGT) images at a resolution of 1 kilometer, ranging from January 2000 to December 2010. They then derived EVI from the four main spectral bands of these images. All four studies used EVI rather than NDVI, as EVI uses the more appropriate near infrared (NIR) reflectance, while NDVI is heavily reliant on the red band, which is affected by cloud cover and atmospheric perturbations in the wet season and aerosol contamination in the dry season (Ratana et al. 2006; Moreau and Defourny 2012).

2.5 LITERATURE REVIEW SYNTHESIS

This literature review sought to summarize the current research on the review questions. Research on the importance of the Amazon is extensive and shows that the Amazon plays a key role not only as a biodiversity hotspot, but also as a carbon sink due to its role of regulating the earth's climate, with yearly phenological patterns playing an important role in the timing and effectiveness of the Amazon's carbon uptake. Research has also focused heavily on urban growth, agricultural expansion and logging as drivers of deforestation and land cover change, with studies estimating that deforestation in the Amazon began to accelerate from the mid 1960's firstly by state-driven urban expansion, and then even further due to agricultural expansion for beef production in the 1970s, and soybean production in the 1990s. More recent studies also showed that mining appeared to be a major driver of deforestation, which started with the 1970s gold rush in Brazil and was further fuelled by the 2008 global recession when the price of gold spiked. Research shows that mining alters the composition of the forests that have been exposed to mining, and causes serious impacts to forest structure through forest fragmentation. Research papers on the effects of fragmentation on forests showed that mining and its associated secondary infrastructure such as roads not only lead to an increase in the number of patches and decrease in the average area of patches, but also threatens plant species diversity, especially near the edge of fragments.

Remote sensing methods for detecting mining in the Amazon rely upon land use land cover classification algorithms, predominantly using Landsat images. While remote sensing first began to be used for mining detection in the Amazon in 2002, the use of more advanced algorithms started with the use of the spectral unmixing classification algorithm in the CLASLITE program by Asner et al. (2013). This well-established methodology was widely used throughout the years, eventually being improved by Caballero Espejo et al. (2018), who added a semi-automated post classification step to address the problem of under-classification present in the original spectral unmixing approach. Lobo et al. (2018) diverted from this approach and was one of the first to use new cloud processing technologies in GEE in an attempt to improve mining detection methods. While this approach sped up the initial classification, their study still relied upon manual reclassification for the post-classification stage, ultimately falling short of the more automated post-classification approach by Caballero Espejo et al. (2018). To date, there is no documented method that combines both cloud processing for the initial classification and an automated model for post-classification in the same methodology.

Assessing the impact of mining on forest structure through fragmentation relied upon the use of metrics capable of quantifying the extent of fragmentation. Over the years, dozens of fragmentation metrics have been used, with many being based on the Ritters et al. (2000) model. Other promising methods include the effective mesh size developed by Jaeger (2000), which was subsequently used in many other studies. Methods to assess phenological changes as a result of a disturbance such as mining all used MODIS images and the enhanced vegetation index (EVI). Depending on the availability of data before a disturbance event, studies either used the temporal or contextual methods.

Overall, early research on land cover change in the Amazon was mainly focused on the impacts of well-known drivers such as logging, agricultural expansion and urban growth, while very little focus was placed on mining. It is only in the last decade that mining began to be studied in more detail, with many papers being published on the impacts of mining on forest cover in the Madre de Dios region of Peru and parts of the Brazilian Amazon. Apart from Peterson and Heemskerk (2001) and Rahm (2015) there has been no other research (to the best of my knowledge) that has focused on the impacts of mining in the northern Amazon in the region of Guyana and Suriname. Not only is there a strong need for research in this area, especially after the period of 2001, but there is also a need for more advanced and updated methods for mining detection which incorporate both cloud processing and automated classification models, both of which this study will seek to address.

3. OBJECTIVES

This study addresses four research objectives:

1. To improve existing LU/LC classification techniques for mining detection through the development of a cloud processing based, semi-automated approach to the mining detection process;

2. To quantify the increase of industrial mining and ASGM and its impact on forest cover between 1997 and 2019 in the Suriname Amazon rainforest;

3. To evaluate the impact of mining expansion on forest fragmentation in industrial mining vs ASGM sub regions; and

4. To analyse the impact of mining expansion on the phenology of the forest ecosystem in industrial mining vs. ASGM vs natural sub regions.

4. STUDY AREA

The study area is in the South American country of Suriname, which has a population of 612 000 and an area of 163 000 km². Suriname is located entirely in the northern portion of the Amazon basin, and the Amazon rainforest makes up 98.3% of the country's total area, making it the most forested country in the world (Miller 2019). However, the rising number of industrial and artisanal mines presents a threat to the quantity and quality of forest cover. Suriname is currently ranked 10th globally in mining production relative to area (Amazon conservation team 2022). The study area (figure 2) encompasses 4 Landsat tiles that are located in the area of the country where the overwhelming majority of mining is located, and where the largest growth is concentrated. The study area covers 43% of the country of Suriname. For the fragmentation and phenology analyses, 3 smaller sub areas were used.
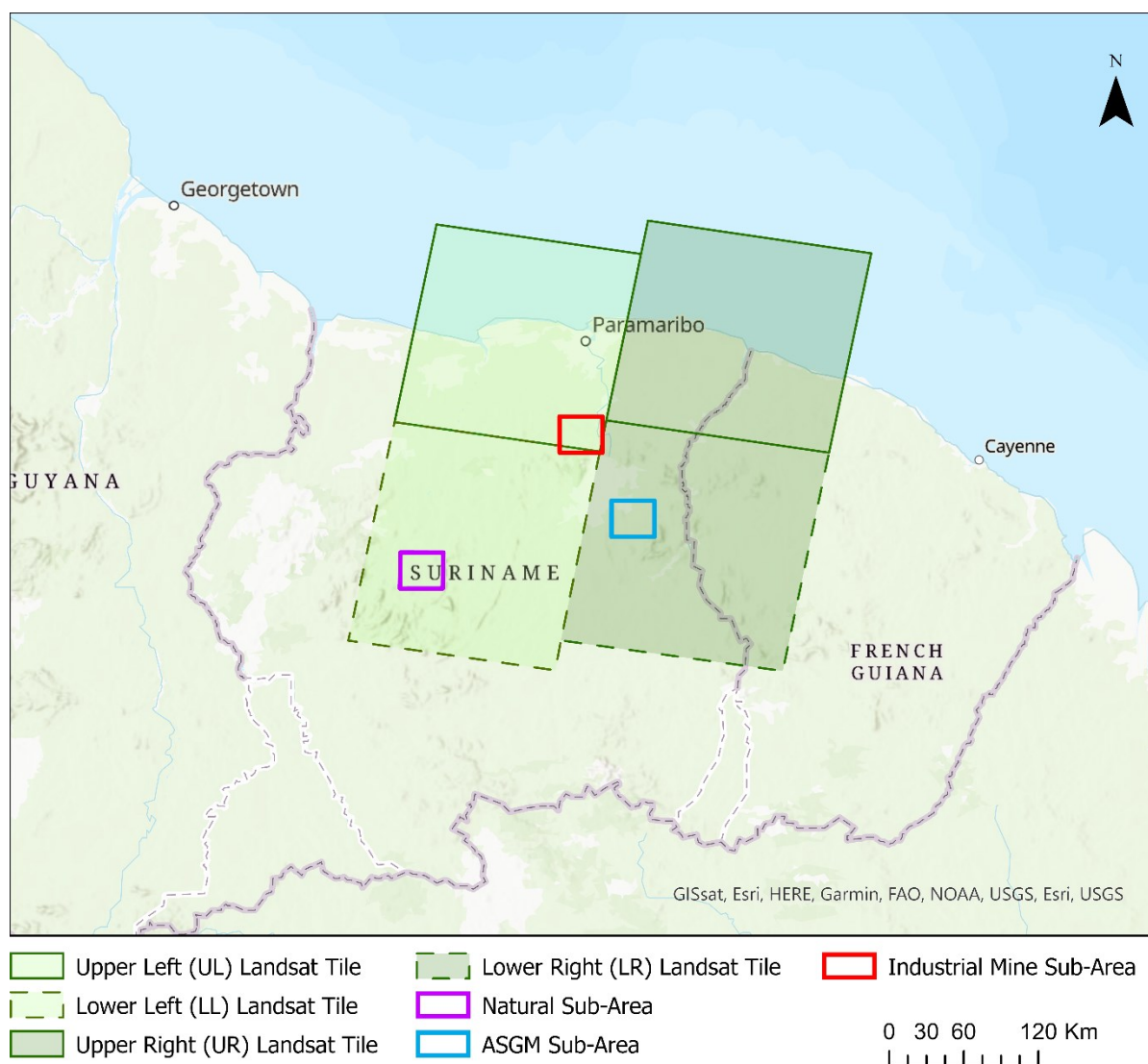

Figure 2. Map showing the location of the study area

5. DATA AND METHODS

The methodology for this study is summarized according to the 4 objectives (Figure 3).
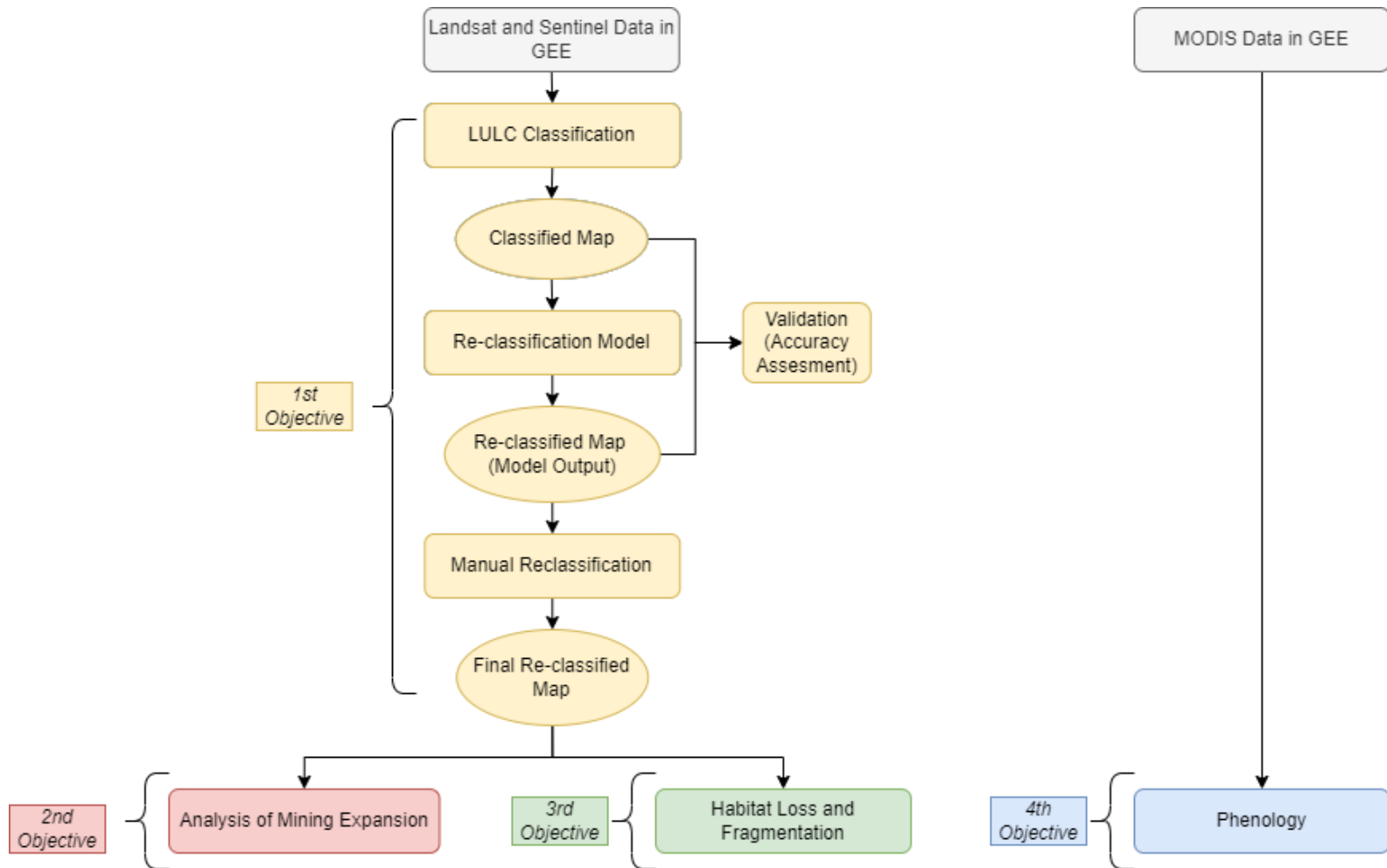

Figure 3. Simplified flowchart showing the flow of methods

5.1: LULC CLASSIFICATION (GEE)

5.1.1 Platform

The first step of this study, which forms the basis of all the supplementary analyses, is the initial land use / land cover classification. This was done using Google Earth Engine, a cloud processing platform which provides a public catalog containing petabytes of satellite imagery and geospatial datasets, allowing for high performance and rapid planetary scale processing and analysis of images (Gorelick et al. 2017). This platform was chosen as the large scale at which this study is conducted (covering almost the entire country of Suriname and 4 Landsat Tiles) necessitates a platform which allows for ease of access to large data files which can be rapidly processed. The use of GEE is corroborated by Lobo et al. (2018), who found that GEE proved to be a cost-effective method in terms of both time and resources as it allows for access, selection and processing of satellite images in seconds to minutes, compared to the hours it would take using other databases such as the USGS website.

5.1.2 Data

The first step in GEE was to import, filter, and display the Landsat images. For this study, Landsat 5 (USGS Landsat 5 Level 2, Collection 2, Tier 1) and Landsat 8 (USGS Landsat 8 Level 2, Collection 2, Tier 1) images were used. Landsat is a joint USGA/NASA program which has been launching satellites for the purpose of earth observation for the last 40 years. Landsat satellites record the earth at a 30 meter resolution and have a 16 day repeat cycle. While alternate sources of data such as Sentinel and the Moderate Resolution Imaging Spectroradiometer (MODIS) were also options, Landsat data proved to be the most suitable for the context of this study. As the study sought to fill a gap since the last research paper by Peterson and Heemskerk in 2001 and analyse the growth of mines in the 21st century, especially with the mining boom that followed the 2008 financial crisis, data that was available from at least the early 2000s was required. Sentinel Images, as used by Lobo et al. (2018) while boasting a higher spatial resolution of 10m, was only launched in 2014 and therefore does not cover a span of time long enough for the purposes of this study. Such a short time period would not have given enough data to analyse the trends in mining growth. MODIS on the other hand, while having launched earlier in 1999, provides data at a spatial resolution of 250 meters, which was too coarse to accurately classify the growth of mining regions. Landsat therefore provided an excellent balance between time period covered and a

resolution high enough to accurately classify mining regions. For mining studies, while higher resolution images (e.g. 10 m) are preferred for the identification of the smallest mine components, images with resolutions of 30 m are capable of accurately identify mines and their clearly identifiable larger components such as pools of water, patches of vegeation and bare soil. Images with lower resolutions (e.g 250 m) fail to identify mining components, making them unsuitable in mining studies. The use of Landsat images at a 30 m resolution is consistent with the approach of the majority of remote sensing mining studies conducted in the Amazon rainforest (e.g. Almeida-Filho (2002), Charou et al. (2010). Elmes et al. (2014), Caballero Espejo et al. (2018) and Nicolau et al. (2019). All of the data for this study used the WGS 1984 UTM Zone 21N coordinate system.

5.1.3 Data Collection and Preparation / Pre-Processing

After the Landsat image collections were imported into GEE, the images were filtered in order to reduce the collection to the most suitable images. The images were firstly reduced by region, whereby only images over the study area (which encompassed 4 Landsat tiles) were selected. Subsequently, the images were then reduced according to their cloud cover (each image reported a pre-calculated value for % cloud cover) , where only images within the study area with less than 10% cloud cover were selected. Finally, only the years in which all 4 Landsat images in the study area met the threshold of <10% cloud cover were selected. From these available years, the 3 years of 1997, 2009, and 2019 were chosen. This time period met the goal of filling a 2 decade long research gap since the last paper on mining in Suriname by Peterson and Heemskerk was published in 2001. The use of an intermediate time step in 2009 allowed for a more detailed analysis of the rate of change between the base year of 1997 and the final year of 2019. Landsat 5 was used for the 1997 and 2009 images, with Landsat 8 being used for 2019.

The 4 best Landsat images in each year were chosen. These were selected as the images with the least cloud cover (especially over the known mining hotspot areas near the Brokopondo reservoir). The dates of the 1997 images (Landsat 5) ranged from August to October. The 2009 images (Landsat 5) ranged from ranged from August to November. Due to constraints with cloud cover in the 2019 images (Landsat 8), 3 were from September to October 2019 and one (lower right scene) was from 2020. A total of 12 Landsat images (4 for each of the 3 years) were used. To avoid persistent cloud cover over the rainforest, all images were collected from the dry season in Suriname, which runs from mid-August to late November.

The 4 images for the first time period (1997) were combined to form an image collection for that year. This was repeated for the other 2 years in the study, resulting in 3 image collections.

5.1.4 Cloud Masking

Based on the image quality band, a cloud mask for each of the 4 images was then created, where clouds were assigned a value of 0, and all other cloud free regions a value of 1. This was done using the GEE cloud masking algorithm. This was done for all 4 images in each of the 3 years, resulting in 12 cloud mask files. These files were used solely for visualisation in the following steps and not as inputs to the unsupervised and supervised classification. The unsupervised and supervised classification in the following steps was done on each of the 12 Landsat scenes used in the study separately and this step was repeated 12 times.

5.1.5 Unsupervised classification

Unsupervised classification was firstly conducted on the images. Unsupervised classification serves to automatically separate pixels in the image into distinct spectral groups. The unsupervised classification algorithm used was the K means clustering algorithm (known as ee.Clusterer.wekaKMeans in GEE), which segmented the image into 10 classes. 10 classes were chosen as this number doubled the amount of classes to be used in the supervised classification (5), and therefore allowed for an initial assessment of the study area and the identification of sub-class spectral patterns that existed within each of the 5 final classes. This provided crucial information which allowed a more informed decision to be made as to which areas were most suitable to place training sites for the supervised classification. The unsupervised classification map was produced solely for the purpose of visualisation for the supervised classification and was not exported.

5.1.6 Supervised Classification:

Selection of LULC classes and training sites:

The first step in the supervised classification was the selection of the LULC classes to be used in the algorithm. 5 classes (mines, water, forest, urban areas, and bare soil) were selected. These 5 classes

reflected all the major LULC classes present in the area and were spectrally distinct enough to allow them to be easily discerned and classed separately from each other. Within each of these 5 classes, the spectral signature was homogenous enough to justify the need for only one class per LULC type. For example, for the mining class, even though the study area had not only gold mines but also a small bauxite mine, these areas displayed very similar reflectance properties in the unsupervised classification, justifying the need for only one class for all mines in the area.

The next step was the selection of training sites. Due to the vast, remote and dangerous nature of the study area, it was not feasible to collect training data through fieldwork. A lack of high-resolution imagery available for many of the earlier points in time meant that the original Landsat imagery along with the unsupervised classification map was used to collect training data. Locations for training sites were chosen by using a.) the scaled Landsat image collection from step 5.1.3 which was used as a basemap, b.) the cloud mask file created in Step 5.1.4 to avoid clouded areas when training, and c.) the unsupervised classification map produced in step 5.1.5 as a further guide. Seventy training sites in the form of points (each point represents one pixel on the map) were selected for each of the 5 classes, making up a total of 350 points per image. The points were placed using a stratified random sampling approach. Stratified in the sense that 5 sub-groups or land cover classes were analysed, but within each class, the points were placed randomly. In supervised classification, the spectral characteristics of these training sites are aggregated to create a user-defined spectral reflectance group for each LULC class. Each remaining pixel in the image, based on it's spectral reflectance, is subsequently assigned to one of these user-defined groups.

Classification Algorithm:

The algorithm used to classify/assign the remaining pixels into the chosen groups was a decision trees classifier known as the classification and regression trees algorithm (CART). According to Lobo et al. (2018) who used CART as the algorithm of choice to classify mines in the Brazilian Amazon, "CART can be defined as a non-parametric, pixel based classifier that uses the DN levels from the training samples to create a decision tree that subsequently classifies each pixel in the image." The CART algorithm was chosen due to its superior performance compared to many other algorithms on GEE. Farda (2017) for example, conducted a study on ten different machine learning classifiers in GEE (using Landsat 5,7 and 8 images), and found that CART outperformed the nine other LULC classification

methods. Over 3 stages of experiments, CART proved to be the highest performing, most accurate classifier, consistently producing results in the high accuracy range (>90%).

In GEE, the CART algorithm, which is known as ee.Classifier.smileCart, contained two adjustable parameters: MaxNodes and MinLeafPopulation. MaxNodes is the maximum number of leaf nodes in each decision tree, while minLeafPopulation represents the minimum number of points present in a training set in order for nodes to be created. Both parameters were set to the default, null or no limits for the maximum number of nodes, and 1 for the minimum number of points for node creation. Due to the complex nature of the mining regions, misclassifications between mine, urban and water classes were expected, with or without optimized model parameters. It was thus decided to use the algorithm with the default parameters.

The CART algorithm was run on the 1st Landsat image in the 1st time period (1997) resulting in a classified map for that image. The entire supervised classification step was repeated 12 times, until all of the other images in the study were classified as well.

5.1.7 Export/Output

The 12 supervised classification maps produced above, as well as the 12 cloud mask files from step 5 were exported to Google drive, downloaded and used as input to the next step. The final script used to automate all these steps in GEE will be made freely available and shared in the appendix (App. A).

5.2: RE-CLASSIFICATION MODEL (ARCGIS PRO)

5.2.1 The need for automated reclassification models in mining detection

Mines typically contain bare rock that makes up the core of the mine, but also exposed earth and pools of water (Figure 4). The challenge with mining detection is that classification algorithms commonly misclassify the exposed earth and pools of water as urban and water classes, respectively. Most current solutions, such as those employed by Asner et al. (2013), Elmes et al. (2014), Rahm (2015), and Lobo et al. (2018) involve extensive manual reclassification to re-assign these misclassified pixels into the appropriate mining class. This can prove tedious, time consuming, and costly when applied to large areas, which is why automated models are essential in mining studies.
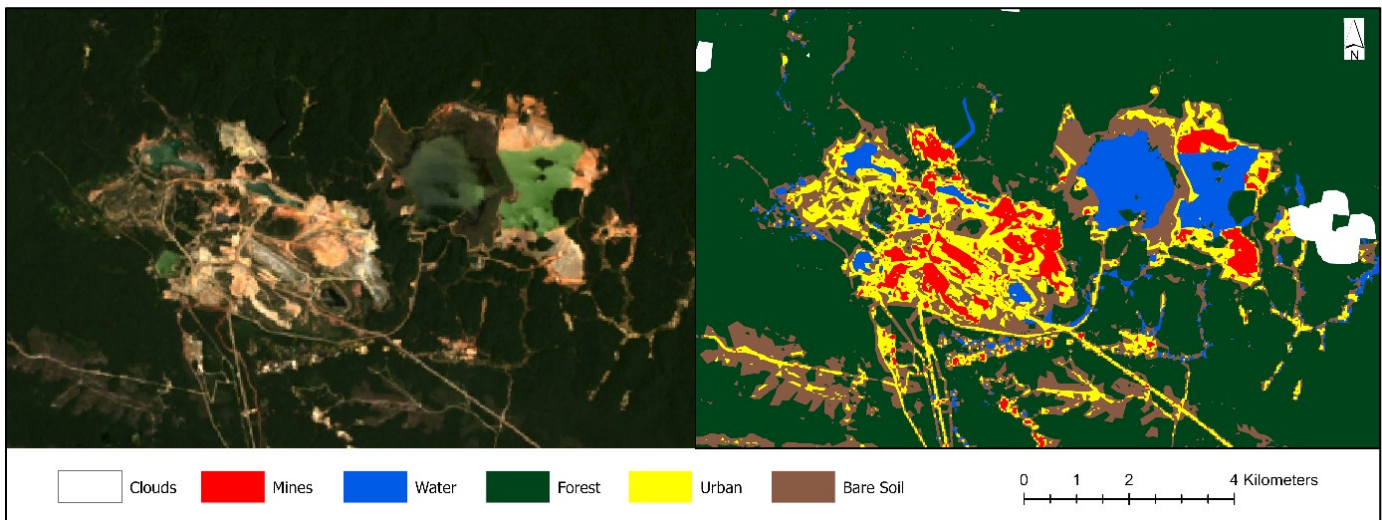

Figure 4: Landsat 8 Image (left) compared to output of CART classification (right)

The output maps of the GEE step were used as input data for the re-classification model. The reclassification model runs on one individual classified map at a time and was therefore run a total of 12 times. The model is separated into 3 sub-models. The first is the cloud masking model, the second is the urban reclass model, and the 3rd is the water reclass model. The output of each sub-model forms the input into the next, with all 3 sub-models running automatically as one overall model, with one output file (figure 5).
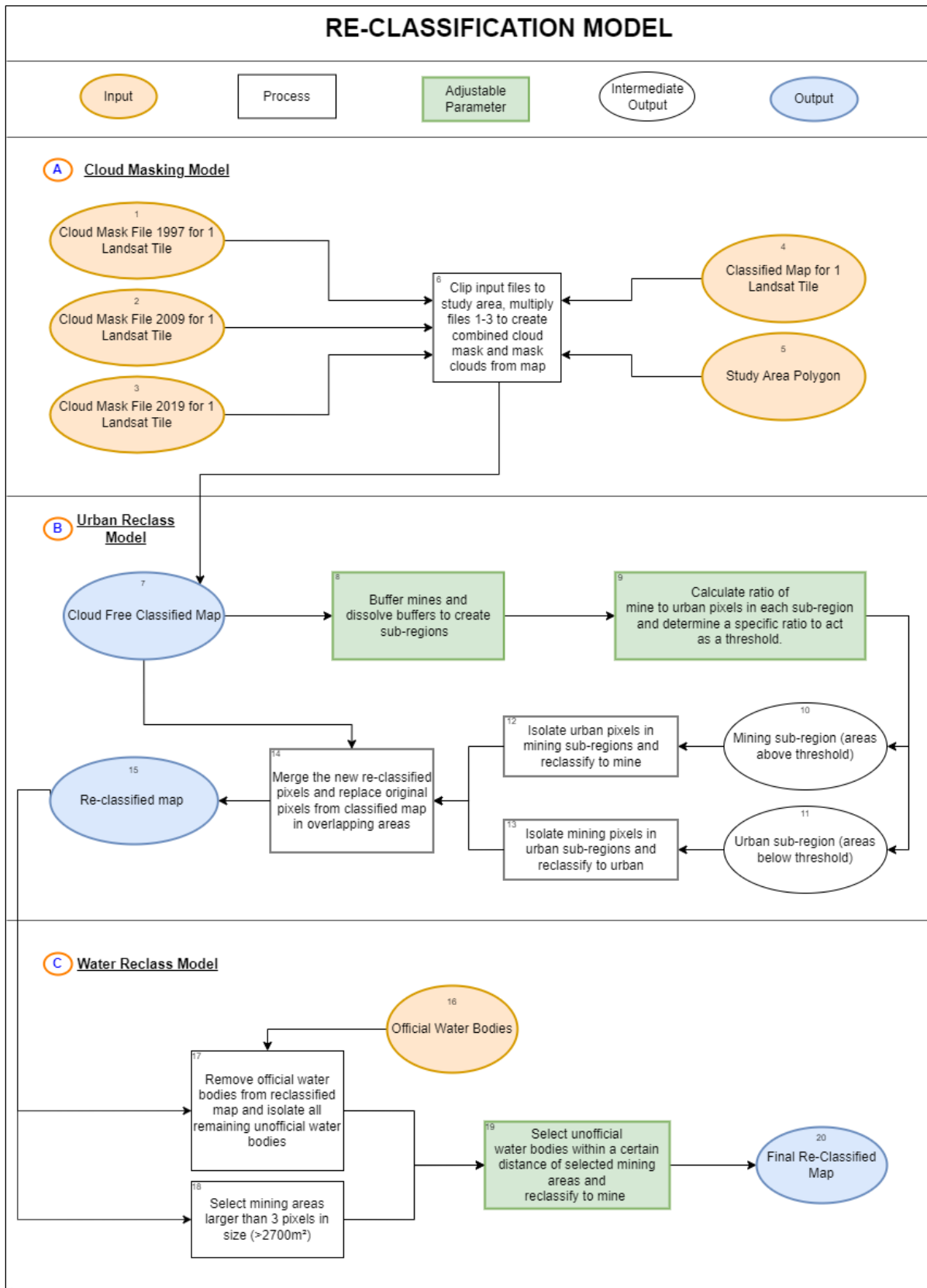
Figure 5: Proposed automated re-classification model.

5.2.2 Model Documentation:

A. <u>**Cloud Masking Model:**</u>

1 to 3. Cloud Mask Files (INPUT) – The first input files to the model were the cloud mask files of 1 Landsat tile for each point in time in the study (1997, 2009, 2019). Three files were used as there were three points in time in the study, and a combined cloud mask highlighting all locations that had clouds in any of the three images needed to be created. The number of input files in this step corresponded to the number of years used in the study. For example, had six points in time been used, the inputs would have been six cloud mask files.

4. Classified Map for 1 Landsat Tile (INPUT) – This model input represents 1 of the 12 classified maps produced from the GEE stage. Each time the model was run on a new classified map, this input was changed. This task was repeated 12 times until each classified maps from the GEE step was run through the model.

4. **Study Area Polygon (INPUT)** – The creation of a study area polygon as an input to the model was a simple but crucial step. This was done as a kind of input control to ensure that the other input files could be clipped to the exact same size and area.

6. Cip and Mask (PROCESS) – In this step, the study area polygon was used to clip the 3 cloud masks and the classified map so that they were all of the exact same size and area. This was necessary as the Landsat 5 and 8 images used came from different satellites which had slightly different swaths, and therefore did not overlap exactly. The study area polygon, therefore, served to remove the edges of the input files where the overlap was not even and create a standard study area to ensure consistency in the comparison of the model outputs over time.

Additionally, the input cloud mask files were combined to create one file which highlighted where all of the clouds across all 3 images were present. For example, if a given area was cloud free in the 1997 cloud mask file but contained clouds in the 2009 cloud mask file, this area would be assigned a value of 0 as containing clouds. This was done to ensure consistency in the comparison of results over time, so that only areas where there were no clouds in all 3 time periods of the study could be compared.

B. Urban Reclass Model

7. Cloud Free Classified Map (OUTPUT) – This output file represents the output of the cloud masking model. It is the same classified map used as input in step 4; however, all areas with clouds have been removed and the map is now the size of the study are polygon specified in step 5.

8. Creation of Sub-Regions (ADJUSTABLE PARAMETER) – This step involved creating a buffer of a specified distance around any pixels classified as mine in the classified map. All overlapping or connected buffers were dissolved to create individual "sub-regions". A sub region can therefore be defined as any separate, distinct region where groups of mining pixels are located in close proximity to each other. This can be a "mining sub-area", which contains groups of correctly classified mining pixels, or an "urban sub-area" which contains groups of incorrectly classified mining pixels. The size of the sub-region depends on the size of the buffer chosen, which varied depending on the input image. For this study, the buffer distances ranged between 100-900 meters. The size of the buffer varied depending on the input image, as this value was dictated by the complexity and potential misclassification of LULC classes in the area. Images with a high complexity of classes, such as the presence of urban areas and mines in close proximity to each other, required a smaller buffer distance to avoid the merging of buffers from two sub-regions in close proximity to each other. Images with a less complex interaction of classes, such as in remote areas of the amazon where an urban class is either non-existent (or is limited to a few small villages) and is not located in close proximity to mining areas, did not require a restriction in the buffer size as there was no risk of overlap between sub-regions. A suitable buffer distance is therefore the value that most accurately identifies and separates the major mining and urban areas into individual sub-regions. Regardless of the buffer distance used, all of the mining and urban pixels within each sub-area were completely captured, ensuring that changes in the size of the buffer did not alter the calculations for any of the subsequent steps.

9. Calculate Ratio of Mine-Urban Pixels and Determine Threshold (ADJUSTABLE PARAMETER) – In each sub-region identified in step 8, the model calculates the ratio of mining pixels to urban pixels and assigns the value to the sub-region. This step of the model was based upon a closely observed pattern in the spatial arrangement of mining and urban pixels. It was

observed that urban areas, while they did contain misclassified mining pixels, were always dominated by an overwhelming majority of urban pixels, hence a low mine-urban pixel ratio. In mining areas, while the mine-urban pixel pattern initially appears to be random, closer observation shows that the ratio of mine to urban pixels within a mine is consistently higher than the corresponding ratio in urban areas. This observed pattern provided the basis for the reclassification model, as it provided a quantifiable metric through which we can consistently distinguish between mining and urban areas.

Once the ratio was calculated for each sub-area, the next step was to observe the assigned values and determine a specific ratio that can act as a threshold to separate mining and urban sub-regions. For example, in a given image (Figure 6), known urban areas such as towns and villages may exhibit ratios between 0.1 and 0.25 (highlighted in white). Conversely, mining sub-regions consistently display higher ratios anywhere upwards of 0.25 (highlighted in brown). A suitable ratio for this image to separate mining and urban sub-regions is therefore 0.25. While threshold values may vary greatly depending on the input image, the principle remained the same; urban areas consistently displayed lower ratios than mining areas and can be distinguished once a suitable threshold is identified.
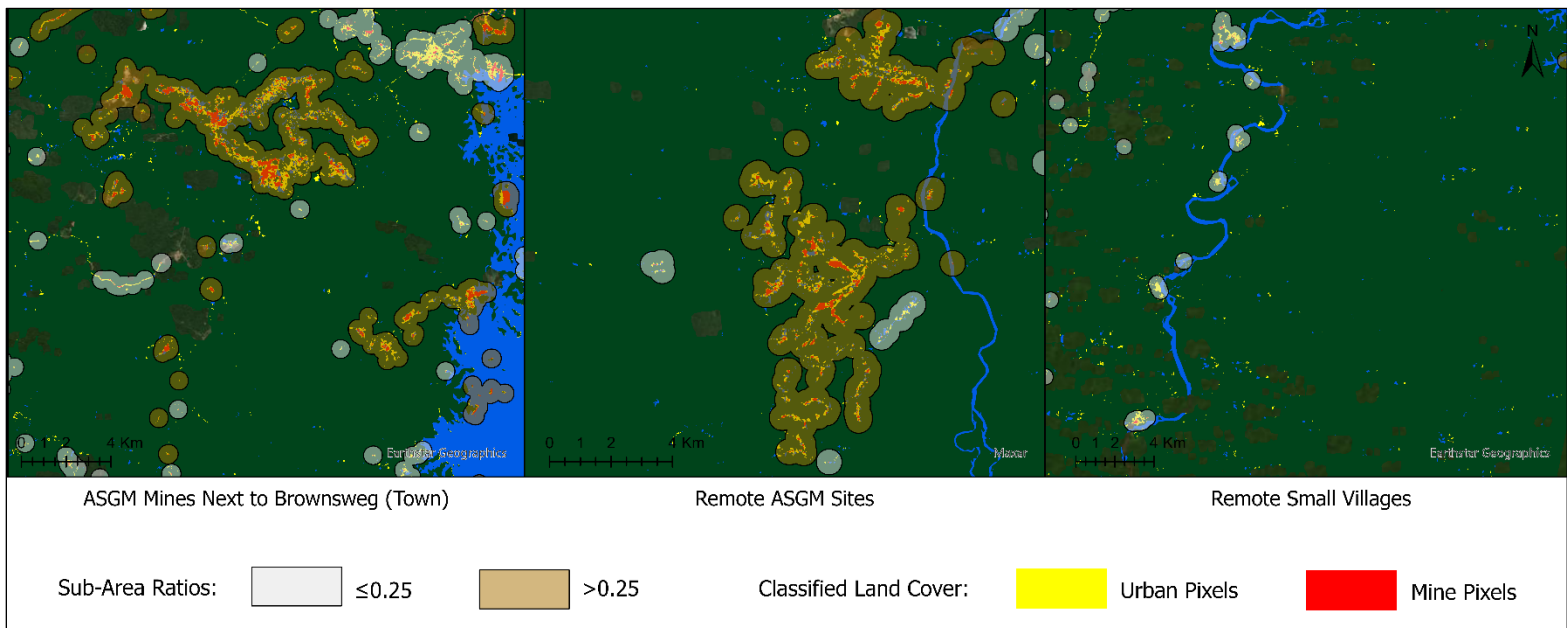

Figure 6: Map highlighting examples of sub-areas created by the model and their assigned ratios. Low ratio (urban) sub-areas are highlighted in white; high ratio (mining) sub-areas in brown.

10-11. Mining Sub Regions and Urban Sub-regions (INTERMEDIATE OUTPUT) –
Following the selection of a threshold, the model split the sub regions into sub-regions that were
below the specified threshold (these were categorised as "urban sub-regions", and regions that
were above the specified threshold (these were categorised as "mining sub-regions".

12-13. Isolate and Reclassify Misclassified Pixels (PROCESS) - The next step was to isolate
the misclassified pixels in these areas and reclassify them to the appropriate class. For example,
urban pixels located within mining sub-regions were isolated and reclassified to the appropriate
mining class. Likewise, any misclassified mining pixels located within urban sub-areas were
reclassified to the appropriate urban class. Any mining pixel in an urban sub-areas was deemed a
misclassified pixel, and likewise any urban pixel within a mining sub-area was deemed a
misclassified pixel, and subsequently reclassified.

14. Replace Original Pixels with Reclassified Pixels (PROCESS) – In overlapping areas, the
original pixels were replaced with newly re-classified pixels.

15. Reclassified Map (OUTPUT) – This output file represents the output of the urban reclass
model, where all the misclassified pixels within the designated sub-regions were assigned to the
correct class.

C. **Water Reclass Model**

16. Official Water Bodies (INPUT) – The final input to the model is a layer representing all the
official water bodies in the study region. This file is crucial to the success of the water reclass
mode, and can be either isolated from the re-classified map produced in step 15 or obtained from
free external sources such as Open Street Map, etc. For the purposes of this study, the prior

method was chosen, and the official water bodies were obtained from the re-classified map. These areas were visually identified by using underlying high resolution satellite imagery as a basemap. This basemap was used solely to visually identify and verify the location of any rivers, lakes, wetlands, or other official water bodies that were classified in the reclassified map. Once these areas were identified, they were manually selected from the re-classified map, isolated and extracted to form a separate layer named "Official Water Bodies".

17. Remove Official Water Bodies and Isolate Unofficial Water Bodies (PROCESS) - Once the official water bodies had been identified, the next step was to remove the official water bodies from the layer with all the water bodies in the area. This left the map with all the remaining water bodies that did not make up rivers, lakes or wetlands. These included pools of water located in the forest for example, such as pools of water in exposed mining pits (which is the target water body for the water reclass model), as well as other unidentified pools of water. These were deemed "unofficial water bodies" and were isolated to ensure that only these water bodies were included in the water reclass model, to ensure that none of the official water bodies such as rivers or lakes were incorrectly reclassified.

18. Select Mining Pixels Above 3 pixel sizes (PROCESS) - In order to remove the influence of isolated, small, misclassified pixels (that are usually 1-2 pixels in size), the minimum size of a mine for this step of the model was deemed as 3 pixels in size (or >2700 m² in a Landsat Image). It is a common occurrence in LULC classification maps, especially those done on a large scale, to contain isolated, misclassified individual pixels. Therefore, only mines above 2700 m² were selected, removing the influence of small, misclassified pixels on the reclassification of water bodies to ensure the most accurate result could be achieved.

19. Proximity of Water Bodies to Mine Function (ADJUSTABLE PARAMETER) - With problematic areas (small, misclassified mining pixels and official water bodies) having been removed, the remaining areas of interest (mining areas above 2700 m² and unofficial water bodies) were selected for further use in the model. For this stage of the model, a proximity function was used to identify water bodies that were within a specified distance of mining regions above 2700 m². This was done to isolate pools of water that collected in exposed pits of mines. These pools of water would be in a mining region and therefore either directly adjacent to or in

very close proximity to other mining pixels. By setting a very small distance (150 m was used for this model) these pools of water could be distinguished from other pools of water that were present in forested or other areas on the map. This is an adjustable parameter than can be tweaked accordingly, however the best results were attained when a smaller distance (< 200 m) was used. The selected pools of water located within the specified distance of mines were isolated and reclassified to mine.

20. Final Reclassified Map (OUTPUT) – This output file represents the final output of the water reclass model. It is also the final output of the entire model.

Final Notes: The entire model, which runs on one classified map at a time, was re-run a total of 12 times until all the initial classified maps from the GEE step were reclassified. The model worked best when it was run with default parameters (buffer distance 100 m, threshold 0.25, water distance to water bodies 150 m) the first time, and the results were observed. This was done in order to get an idea of which model parameters were most suitable for the study area. Once the suitable parameters were identified, they were adjusted to suit and the model was re-run using the corrected parameters. It was noted that the model parameters tended to change for Landsat Images of a different area. This was due to the geography of the area, and whether it was predominantly urban, semi-urban, or rural. Landsat images containing major urban areas such as large cities, airports, and towns required a small threshold value (below 0.5) to split mining regions from urban regions. Conversely, Landsat images in remote rural areas required much higher threshold values (above 1). While parameters changed across images in different areas, different images over time in the same study area used the same parameters, as the geography of each Landsat image (whether it was urban vs rural) remained relatively consistent over time. The adjustable parameters were therefore influenced by a change in location rather than a change over time.

5.3 VALIDATION

After the model was run on the 12 classified images, the next step was to conduct a validation assessment. Validation was conducted on both the 12 re-classified output maps from the model and on the 12 initial classification maps that were exported from GEE before they were run through the model. The validation phase involved conducting an accuracy assessment on the classified maps (before the model) and the re-classified maps (after the model) and comparing the results to get quantifiable data as to how well the reclassification model performed. The large scope of this study (12 Landsat images spanning over 2 decades) provided an ideal platform to test the performance of the model.

The validation data was collected in the form of points in Google Earth Engine. For the 1997 and 2009 images, the lack of high-resolution satellite images available in those time periods meant that the original Landsat 5 images (30-meter resolution) from both time periods were used to collect validation points. For the 2019 image, validation points were collected using high resolution Sentinel images at a 10-meter resolution. The sampling approach for the validation points was stratified random sampling. Stratified in the sense that 5 sub-groups or land cover classes were analysed, but within each class, the points were placed randomly. Validation points were collected for each of the 5 classes, and in total, for all 12 images, 3430 validation points were collected. The distribution of validation points was 819 for mines, 768 for urban, 706 for water, 755 for forest, and 382 for bare soil. Bare soil/fallow field land use class was only present in 2 images, and therefore had approx. half the number of points compared to the other classes. For each class, roughly 60 validation points were collected per image. The placement of more points in mining areas followed the same rationale and approach of Rahm (2015), who placed a higher density of points in mining areas in order to increase the probability of detecting errors and misclassifications, making the results for that class more reliable. Placement of validation points in GEE adhered to 2 major rules: 1. That the validation points were located in cloud-free areas, and 2. The points should not coincide with the training points used in the CART classification. Once validation points were suitably placed, they were then exported from GEE into ArcMap, where the accuracy assessment of the classified maps from GEE and the re-classified model outputs took place.

In ArcMap, a very simple model was created to compare the locations of the validation points to the corresponding LULC classes in the classified map. This model worked on 1 map at a time. This model compared the location of each of the 5 classes for the validation points against each of the 5 classes in the classified Map. For example, for the validation points collected for the mining class, the model determined which classes in the classified map (mining, urban, water, forest, etc.) each of these validation

points ended up in. This process was done for all the classes in the map. The model counted the number of points from each class in the validation data that ended up in each corresponding class in the classified map, and exported these values to Excel, where an error matrix was created in order to get the final statistics for the accuracy assessment.

In Excel, the error matrix was used to calculate the number of points from the validation data that ended up in the correct corresponding class in the classified map. This was used to calculate the overall accuracy of the classified map, which was expressed as a percentage. Additionally, the user accuracy, which is the accuracy of the map from the perspective of a map user, and producer accuracy, which is the accuracy of the map from the perspective of the map maker was also calculated for the mining class alone. This accuracy was expressed as a percentage in order to see how the model performed in reclassifying mines (which is what it was built to do). While the model was built to reclassify mines, it also performed the combined role of reclassifying misclassified mining pixels in urban areas, and therefore also improved the accuracy of the classification of the urban class. The user and producer accuracies of the urban class were also calculated and expressed as a percentage. This process was repeated for each of the 12 images for the classified maps exported from GEE before the model was run. The exact same process was also repeated for the 12 re-classified maps that were produced as an output of the model.

5.4: MANUAL RECLASSIFICATION

After validation was conducted on the data, the re-classified maps underwent one final step before the final maps were produced. This step was a quick manual reclassification in order to remove any major misclassified areas. While the model ensured that the reclassification of mining areas across the map was not necessary as this process was automated, in classification studies, as a form of quality control, it is still important to have the user look over the results and re-classify any major misclassifications. The model therefore does not replace manual re-classification entirely, but rather significantly reduces the length of time it takes by automating the vast majority of the process.

For the manual reclassification, the 4 re-classified maps for each time period were combined to create one large map. This was done for all 3 time periods to create 3 large maps. These maps were then reviewed, and any major misclassifications were removed and reclassified manually. The main misclassified element on the map were areas of shoreline sediment on the banks of the lake, which due to their reflectance properties, were often classified as a mix of either mining or urban areas. Due to the mix of mining and urban pixels within one area, the model often identified these areas as a sub-region, and reclassified them to either mining or urban depending on the ratio of these areas and the threshold used. The misclassified shoreline sediment areas represented 26% of all mining areas but were very easy to identify and reclassify as they were concentrated on the edge of the lake. These 3 final manually reclassified maps of 1997, 2009, and 2019 created in this step were used for all the supplementary analyses (fragmentation and phenology) and calculation of statistics such as growth of mines, forest loss, and growth of Industrial vs. ASGM mines in the entire study area.

5.5 ANALYSIS OF MINING EXPANSION AND FOREST LOSS

The (rapid) manual reclassification ensured that the post-classification statistics calculated in this step were as accurate as possible. Before the statistics were calculated, the locations of the two active industrial mines in Suriname were obtained from the Amazon Conservation Team in Suriname (Amazon Conservation Team 2022). All remaining gold mining areas were ASGM. Subsequently, the areas (in km²) of industrial and ASGM mines were calculated for the entire study area for each of the 3 points in time. A change detection analysis was then conducted to determine the associated forest loss caused directly by both types of mining. The overall forest loss and mining growth for the entire area were also calculated.

5.6 FOREST FRAGMENTATION

The first portion of this step involved the selection of two subset areas of 1000 km² each. These subset areas were rectangles measuring 34.5 km² by 29 km². These two subset areas were chosen in the most concentrated ASGM and industrial mining regions respectively. For these sub areas, the cutting out (CUT) procedure was used, where the boundary of the sub area is considered a barrier. In each subset area, the classified maps of the study areas were surveyed with underlying imagery to determine the presence of fragmenting elements which were disconnected on the maps but connected in reality (as verified in high resolution images). Fragmenting elements refer to all the LULC classes (urban, water, bare soil, mine) in the classified map which contributed to fragmentation of the forest class. Roads, which were also a fragmenting element, were classified as the urban class except when they were located within a mine, where they were classified as the mining class. These fragmenting elements appeared disconnected in some areas due to misclassification. For example, misclassified forest pixels in a road would make the road appear disconnected as two separate parts instead of as one feature. As this would lead to miscalculations, these fragmenting elements were connected where necessary to ensure the calculations of the fragmentation metric of Effective Mesh Size was as accurate as possible. All of the fragmenting elements were then dissolved and added to a separate layer. The forested LULC class was added to another layer. The fragmenting elements layer was then erased from the forests layer to highlight the patches created in the forest class as a result of the fragmenting elements. The effective mesh size for the fragmented landscape was then calculated. Effective Mesh size refers to the size of an area an animal that is randomly dropped into a fragmented landscape would have access to without encountering any fragmenting elements (Jaeger et al. 2007). It was determined by first calculating the probability that any two randomly chosen points in the study area are connected. This value of probability was then multiplied by the size of the study area to get the value for effective mesh size (Meff) in km². The formula for Meff is as follows:

$$m_{\text{eff}} = \left(\left(\frac{A_1}{A_t} \right)^2 + \left(\frac{A_2}{A_t} \right)^2 + \left(\frac{A_3}{A_t} \right)^2 + \ldots + \left(\frac{A_n}{A_t} \right)^2 \right)$$

where n is the number of patches, A_1 to A_n represent the size of the patches from the first patch (A_1) to patch n (A_n), with A_t being the total area of the study region (Jaeger et al. 2007). Effective Mesh size was used as not only is it a single value that is easily interpreted, but "it's reliability has been confirmed on the basis of nine suitability criteria through a systematic comparison with other quantitative measures" (Jaeger et al. 2008). The Effective Mesh size was calculated for all fragmenting elements in the study

area combined, and then was re-calculated with mining areas excluded as a fragmenting element. The influence of mining on the effective mesh size was then directly determined by calculating the difference between the two values.

5.6: PHENOLOGY

The assessment of the forest phenology was done through the peak of season (POS) greenness metric, which was obtained from the Moderate Resolution Imaging Spectroradiometer (MODIS) Land Cover dynamics version 6 data. This data has a spatial resolution of 500 m and includes multiple bands with phenology metrics derived from daily EVI2 measures, including: "onset of greenness, green-up midpoint, maturity, peak greenness, senescence, greendown midpoint, dormancy, EVI2 minimum, EVI2 amplitude, integrated EVI2" (Friedl et al. 2019). The multi-band satellite images from 2001 to 2019 were downloaded through GEE, and the POS metric was calculated for each year as the EVI2 min + EVI2 amplitude (see figure 7 for visualization of the metrics). Annual means and standard deviations of this metric were calculated for the three sub areas (see figure 2 in Study area section) using the zonal statistics tool in ArcGIS Pro (version 2.8.0, ESRI 2021) and changes in the POS values were calculated between 2001 and 2009, 2009 and 2019, and 2001 and 2019.
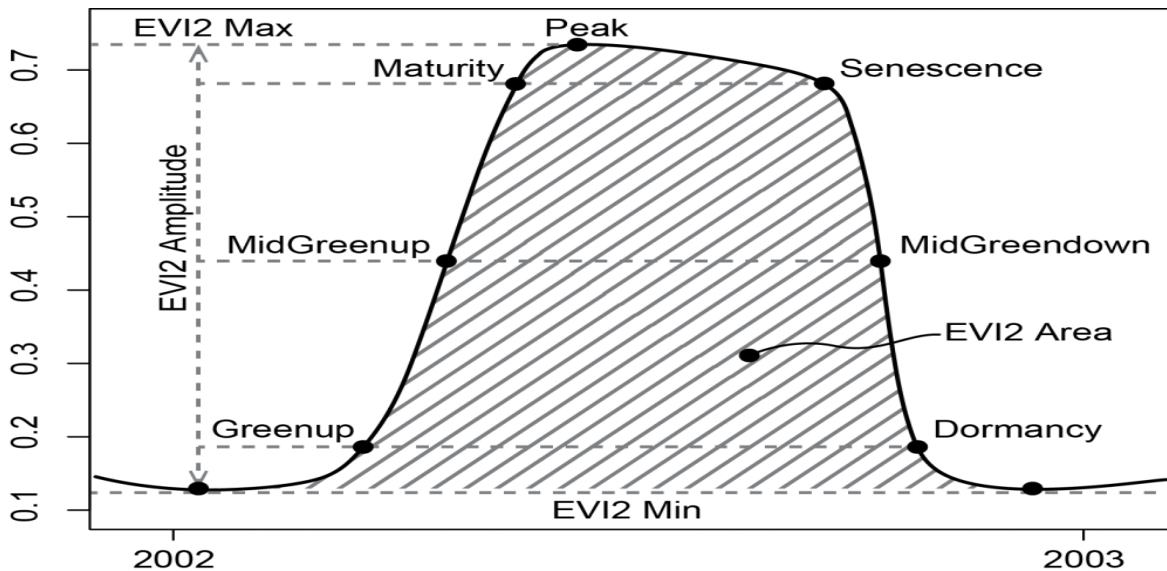

Figure 7: Diagram of MCD12Q2 phenometrics for a hypothetical vegetation cycle. Points indicate times of phenometrics recording (dates) at which EVI2 reached particular fractions of the cycle's overall amplitude. Source: Land Surface Phenology | USA National Phenology Network

6. RESULTS

6.1 RE-CLASSIFICATION MODEL

Table 1 presents the results of the original CART classification, which shows overall accuracies of 84%, 86%, and 81% for the 1997, 2009, and 2019 images, respectively. The average overall accuracy was 84%, with the highest accuracies coming from the water (99% producer accuracy, 94% user accuracy), forest (100% producer accuracy, 93% user accuracy) and bare soil class (77% producer accuracy, 86% user accuracy). The major problematic classes which contributed greatly to a reduction in the overall accuracy were the mining class (65% producer, 79% user accuracy) and urban class (76% producer, 68% user accuracy). These two classes reported lower accuracies than the other 3 classes and were responsible for reducing the overall accuracies of the images across all 3 years. A detailed breakdown of the accuracy of these problematic classes is provided in table 2 below.

Table 1: Overall, producer and user accuracies (in brackets) of Original CART Classification for each of the 3 years.

Year	Water Accuracy (%)	Forest Accuracy (%)	Bare Soil Accuracy (%)	Mining Accuracy (%)	Urban Accuracy (%)	Overall Accuracy (%)
2019	100(82)	99(91)	78(91)	70 (76)	72 (68)	81
2009	100 (99)	100 (92)	78 (90)	69 (81)	78 (72)	86
1997	96 (100)	100 (95)	76 (77)	55 (81)	79 (65)	84
Average	**99 (94)**	**100 (93)**	**77 (86)**	**65 (79)**	**76 (68)**	**84**

Table 2: Producer accuracy, user accuracy (in brackets) and overall accuracy of each image for the original CART classification (before model) compared to the accuracy after application of the re-classification model.

	IMAGE	BEFORE MODEL			AFTER MODEL		
		Overall Accuracy of all classes (%)	Mining Accuracy (%) Producer (User)	Urban Accuracy (%) Producer (User)	Overall Accuracy of all 5 classes (%)	Mining Accuracy (%) Producer (User)	Urban Accuracy (%) Producer (User)
2019	2019 Upper Left	78	52 (60)	58 (58)	93	85 (100)	97 (84)
	2019 Upper Right	84	81 (84)	74 (71)	89	93 (100)	89 (79)
	2019 Lower Left	80	79 (73)	83 (63)	91	88 (100)	89 (91)
	2019 Lower Right	82	67 (86)	74 (81)	96	98 (95)	86 (100)
	Average	**81**	**70 (76)**	**72 (68)**	**92**	**91 (99)**	**90 (89)**
2009	2009 Upper Left	84	65 (92)	87 (60)	93	94 (100)	94 (81)
	2009 Upper Right	78	60 (53)	48 (62)	85	47 (100)	93 (69)
	2009 Lower Left	90	59 (97)	99 (74)	93	70 (100)	100 (81)
	2009 Lower Right	92	93 (82)	77 (93)	95	89 (94)	89 (91)
	Average	**86**	**69 (81)**	**78 (72)**	**92**	**75 (99)**	**94 (81)**
1997	1997 Upper Left	82	59 (98)	83 (76)	86	79 (100)	89 (70)
	1997 Upper Right	83	69 (87)	72 (54)	89	88 (100)	85 (69)
	1997 Lower Left	85	17 (71)	94 (56)	94	100 (74)	69 (100)
	1997 Lower Right	85	73 (66)	67 (74)	90	82 (77)	78 (84)
	Average	**84**	**55 (81)**	**79 (65)**	**90**	**87 (88)**	**81 (81)**
	OVERALL AVERAGE	**84**	**65 (79)**	**76 (68)**	**91**	**84 (95)**	**88 (84)**

The overall accuracy of all classes varied from one image to another for each year. Overall, the lower left and lower right images tended to have higher accuracies than the upper left and upper right. This was due to the land cover complexity of the upper left and upper right images, which were located in a highly urbanized setting, where large towns and cities were present, which made it much more difficult to accurately classify. The complex nature of these images also necessitated the inclusion of a bare soil class. The lower right and left images on the other hand, were much less complex, as they were located in remote, almost fully forested areas, and did not require the inclusion of a bare soil class. The classification therefore covers images with vastly different geographies, which tests the performance of the model in a variety of different settings.

The mining accuracy was lowest in the 1997 images, with an average producer accuracy of 55% and user accuracy of 81%. The mining accuracy for the 2009 images was slightly higher, with a producer accuracy of 69% and user accuracy of 81%. The 2019 images had a producer accuracy of 70% and a user accuracy of 76%. These low accuracies are typical of mining regions given their notoriously high spectral variability (Lobo et al. 2018). As the target class for the semi-automated reclassification model, the mining accuracy in all the images greatly improved after the model was run. The mining producer accuracy in 1997 increased by 32 (55% to 87%), while the user accuracy increased by 7 (81% to 88%). The 2009 images saw an increase of 6 in producer accuracy (69% to 75%) and an increase of 18 in user accuracy (81% to 99%). The model performed at its best for the Landsat 8 images in 2019 (where the extent of mining was greatest) with an increase in producer accuracy of 21 (70% to 91%), and an increase of 23 in user accuracy (76% to 99%).

In addition to the improvements in mining accuracy, the construction of the model and its ability to reclassify misclassified pixels in urban areas led to a concurrent improvement in the urban accuracy across all 12 images. The urban producer accuracy in 1997 increased by 2 (79% to 81%), while the user accuracy improved by 16 (65% to 81%). For the 2009 images, the urban producer accuracy increased by 16 (78% to 94%) while the user accuracy increased by 9 (72% to 81%). The 2019 images saw an improvement in producer accuracy of 18 (72% to 90%) and user accuracy of 21 (68% to 89%).
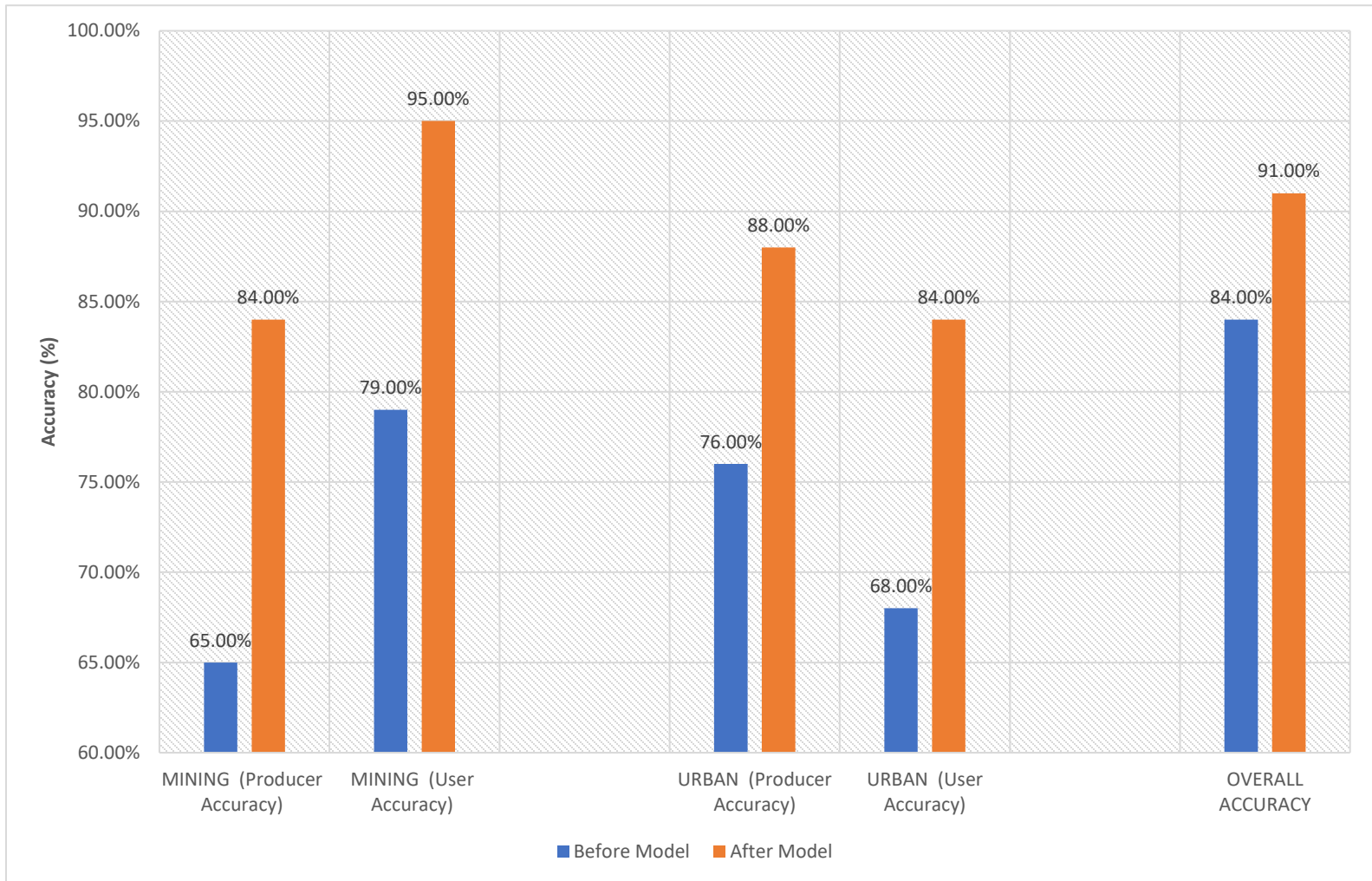
Figure 8: Summary of model performance showing average mining accuracy, urban accuracy and overall accuracy in all three time points.

The combined impact of this improvement of both the mining and urban class led to noticeable increases in the overall accuracy of the classification. As seen in figure 8, the overall accuracy of the classified map increased by 7 from 84% to 91%. The urban producer accuracy increased by 12 from 76% to 88% while the user accuracy increased by 16 from 68% to 84%. The mining class saw even greater improvements, with an increase of 19 in producer accuracy and an increase of 16 in user accuracy after the reclassification.
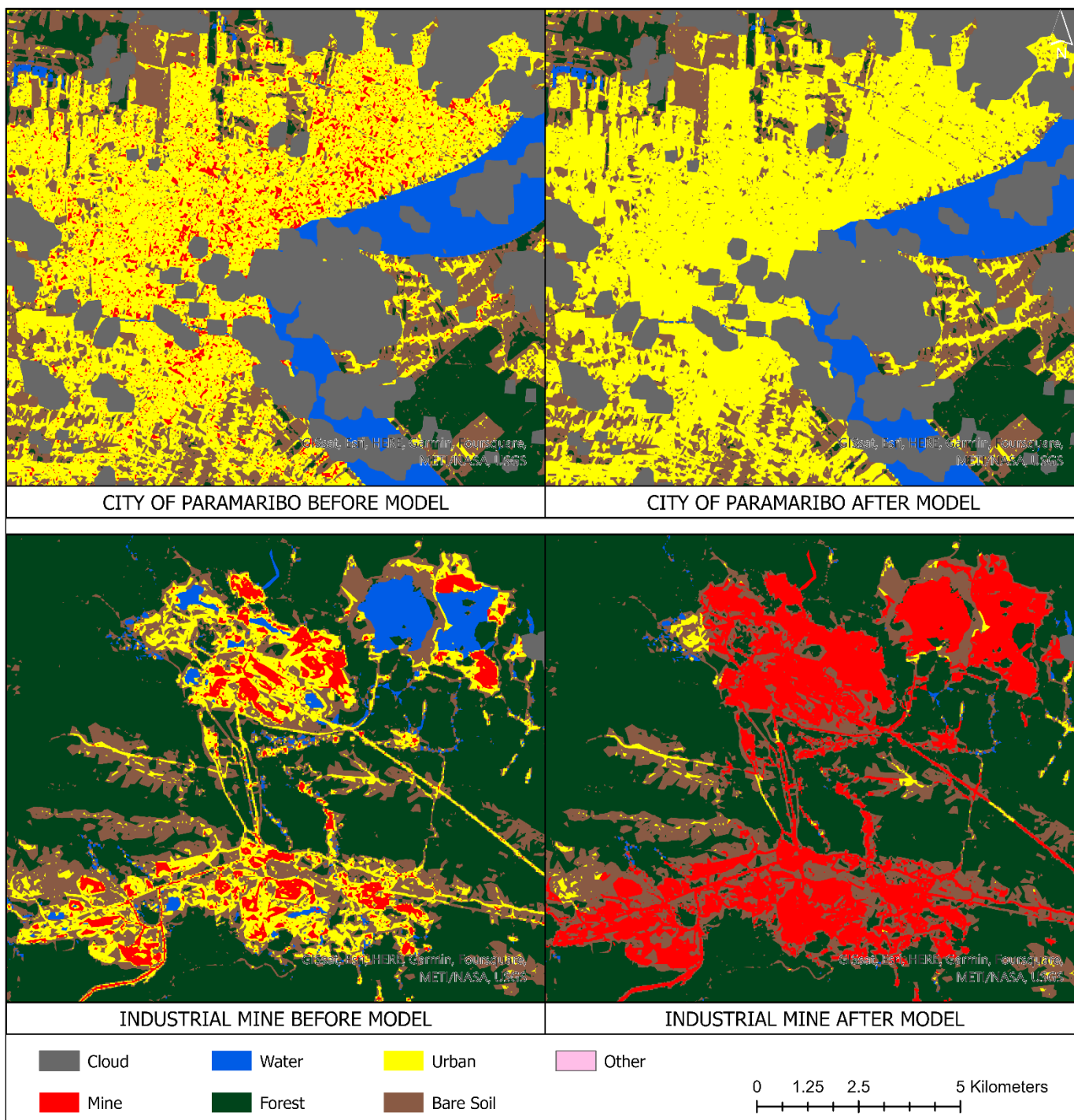
Figure 9: Performance of model in reclassifying the largest mines (such as Rosabel Industrial Mine) and urban areas (Paramaribo)

This improvement in the accuracy of both mining and urban detection is apparent in large, medium, and small mines/urban areas. As seen in figure 9, the model performed well in re-classifying the largest industrial mines and as well as misclassified mining pixels in the capital city of Paramaribo.
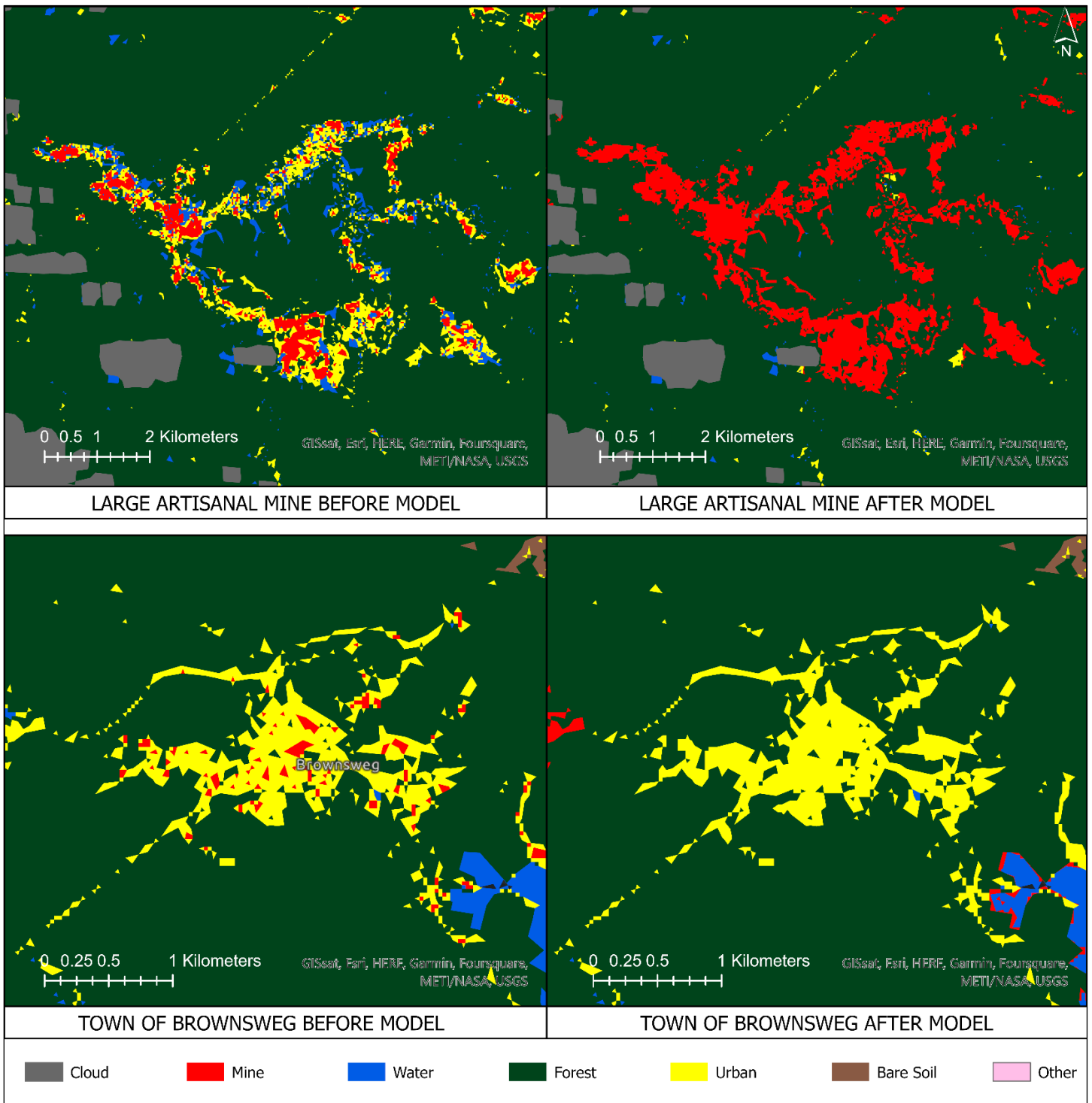
Figure 10: Performance of model in reclassifying medium-sized mines and urban areas

A seen in figure 10, the model also performed well in reclassifying artisanal mines and medium-sized urban areas, successfully reclassifying one of the larger artisanal mines as well as the medium-sized town of Brownsweg.
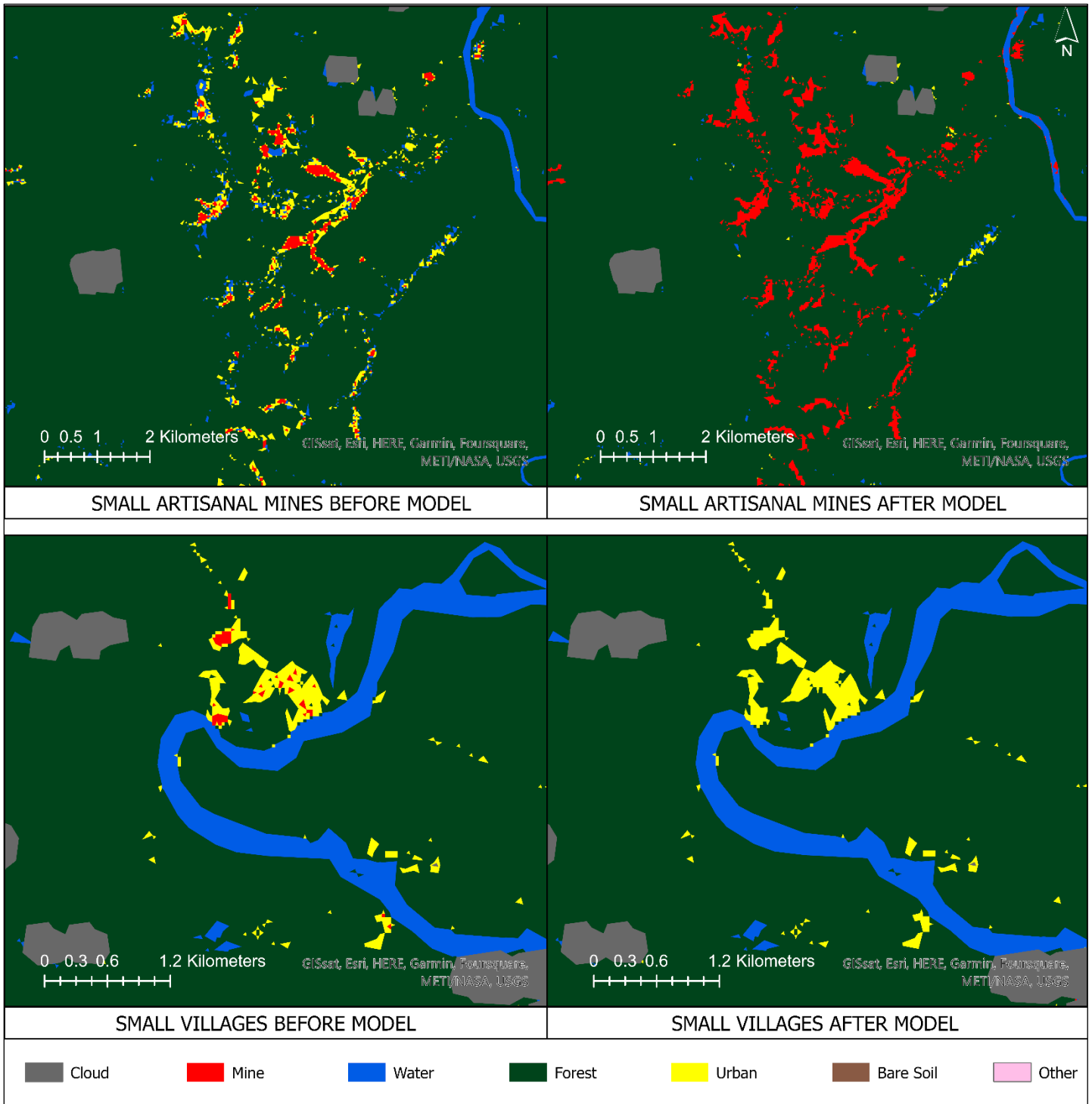
Figure 11: Performance of model in reclassifying the smallest mines and urban areas

The model also showed good performance on even on the smallest mines and urban areas, such as the smallest artisanal mines and villages near the riverbanks (Figure 11). Misclassified pixels in these areas were successfully removed and reclassified into the appropriate mining or urban class.

6.2 MINING EXPANSION AND FOREST LOSS

The two main types of gold mining activities in Suriname (industrial and artisanal mines) are concentrated around the Brokopondo reservoir (figure 12). The two industrial gold mines (Rosabel and Merian mines) are located in the west and east of the study area, while the other gold mining areas are all artisanal gold mines. A very small area of industrial bauxite mining is also present in the north of the study area near the capital city of Paramaribo.
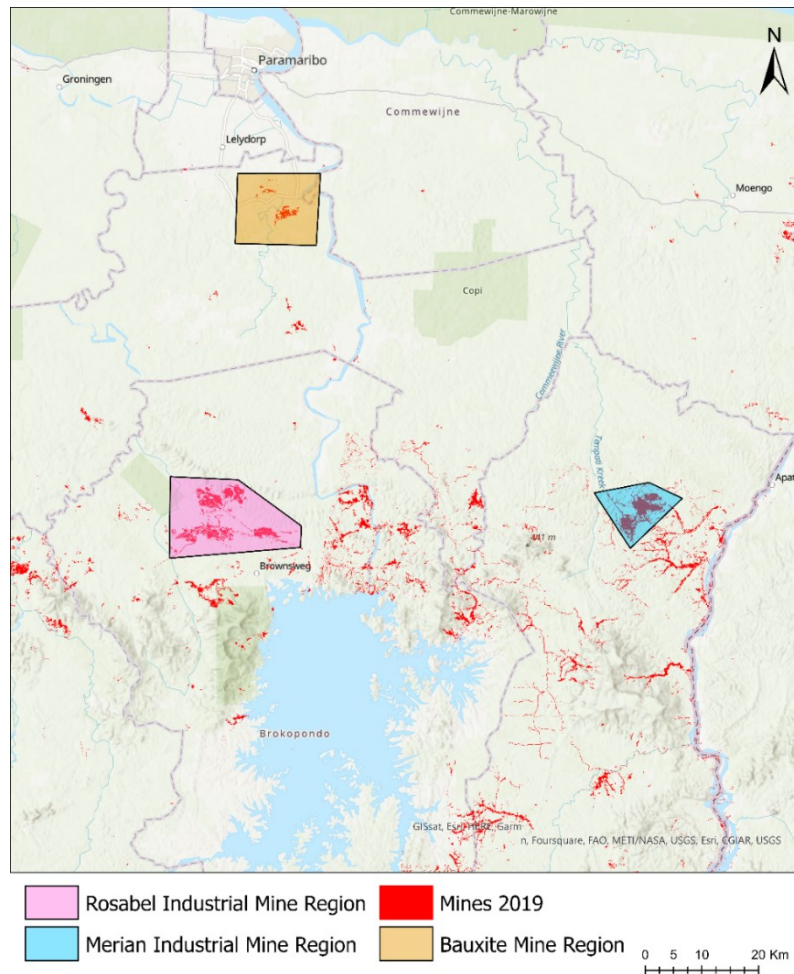

Figure 12: Map of major types of Mining in Suriname

The final classified maps highlight the clear growth of gold mines between the time periods (Figure 13). From 1997 to 2009, there was the noticeable expansion in the development of the Rosabel mine, along with the development of smaller artisanal mines in the southeast region of the reservoir. From 2009 to 2019, there was the inception of the new Merian industrial mine in the northeast, along with a massive development of artisanal mines all over the study area.
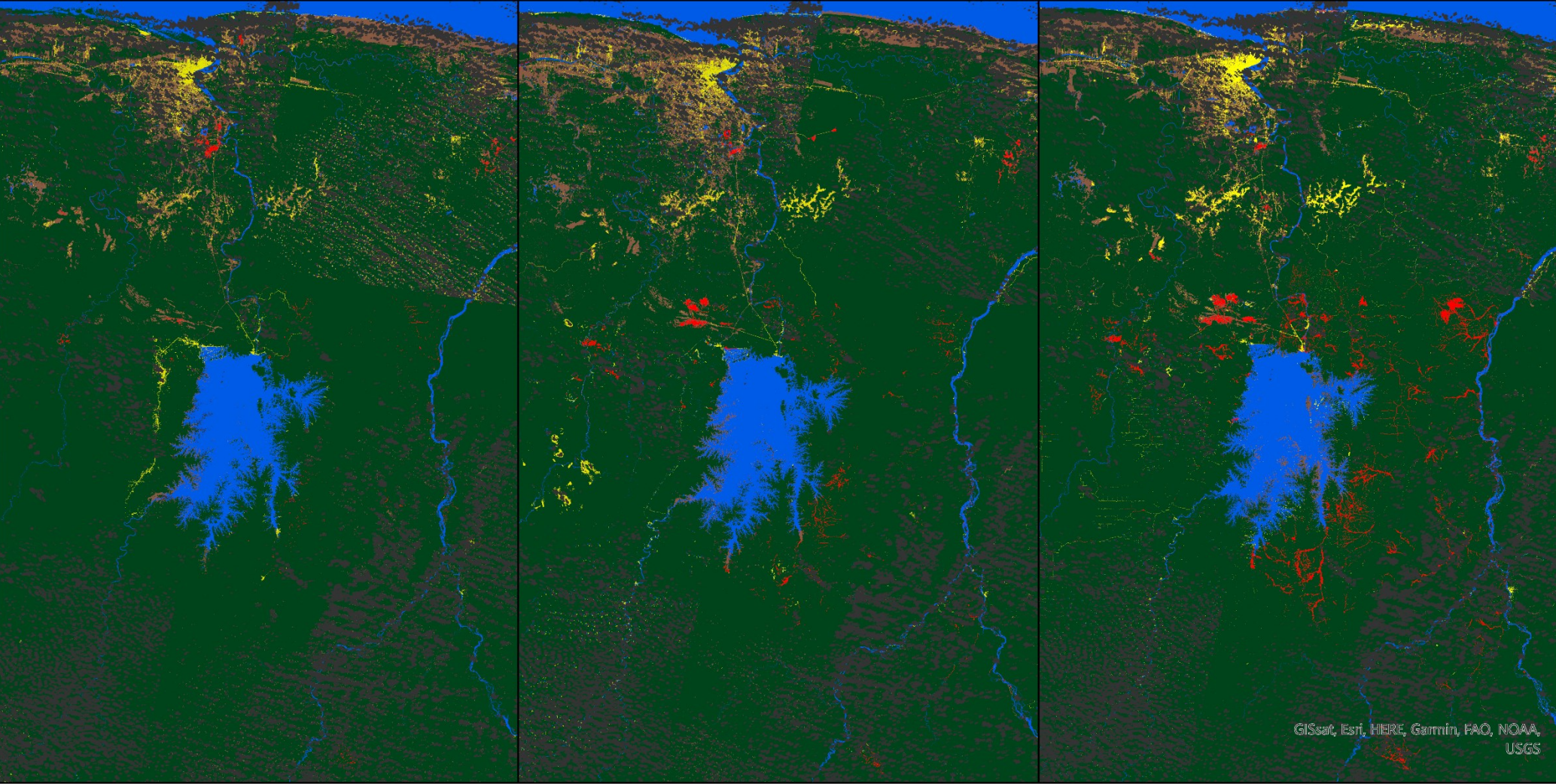
Figure 13: Map showing all final classified maps highlighting mining expansion between 1997 and 2019.

Table 3: Mining growth and net forest loss between 1997 and 2019

	1997	2009	2019
Area of Industrial Gold Mines (km^2)	2	27.5	64.1
Net Forest Loss from Industrial Gold Mines (km^2)	-2	-22.5	-62
Area of Artisanal Gold Mines (km^2)	50.7	117.6	362
Net Forest Loss from Artisanal Gold Mines (km^2)	-50.7	-113.2	-343.9
Area of Bauxite Mines (km^2)	16.7	9.3	5.5
Net Forest Loss from Bauxite Mines (km^2)	-16.7	-15.1	-15.4
Total Area of Mines (km^2)	69.4	154.4	431.6
Total Net Forest Loss from Mining (km^2)	-69.4	-150.8	-421.3

The considerable growth of mining highlighted in figure 11 is quantified in table 3 and can be attributed to the 2 main types of mining: industrial gold mining and artisanal gold mining. Overall, artisanal gold mining dominates the landscape and accounts for 84% of all mines in Suriname in 2019, followed by industrial gold mining, which accounts for 15%. Bauxite mining is also present in Suriname, however, is only present in one area, and has been gradually decreasing in size over the years leading up to it being decommissioned and closed in 2017. Bauxite mining also only accounts for a very small portion (1%) of mining in the region.

Given the lack of data before 1997, the 1997 year was used as a baseline, and the assumption was made that all mining growth leading up to that year was into forested areas and resulted in forest loss.
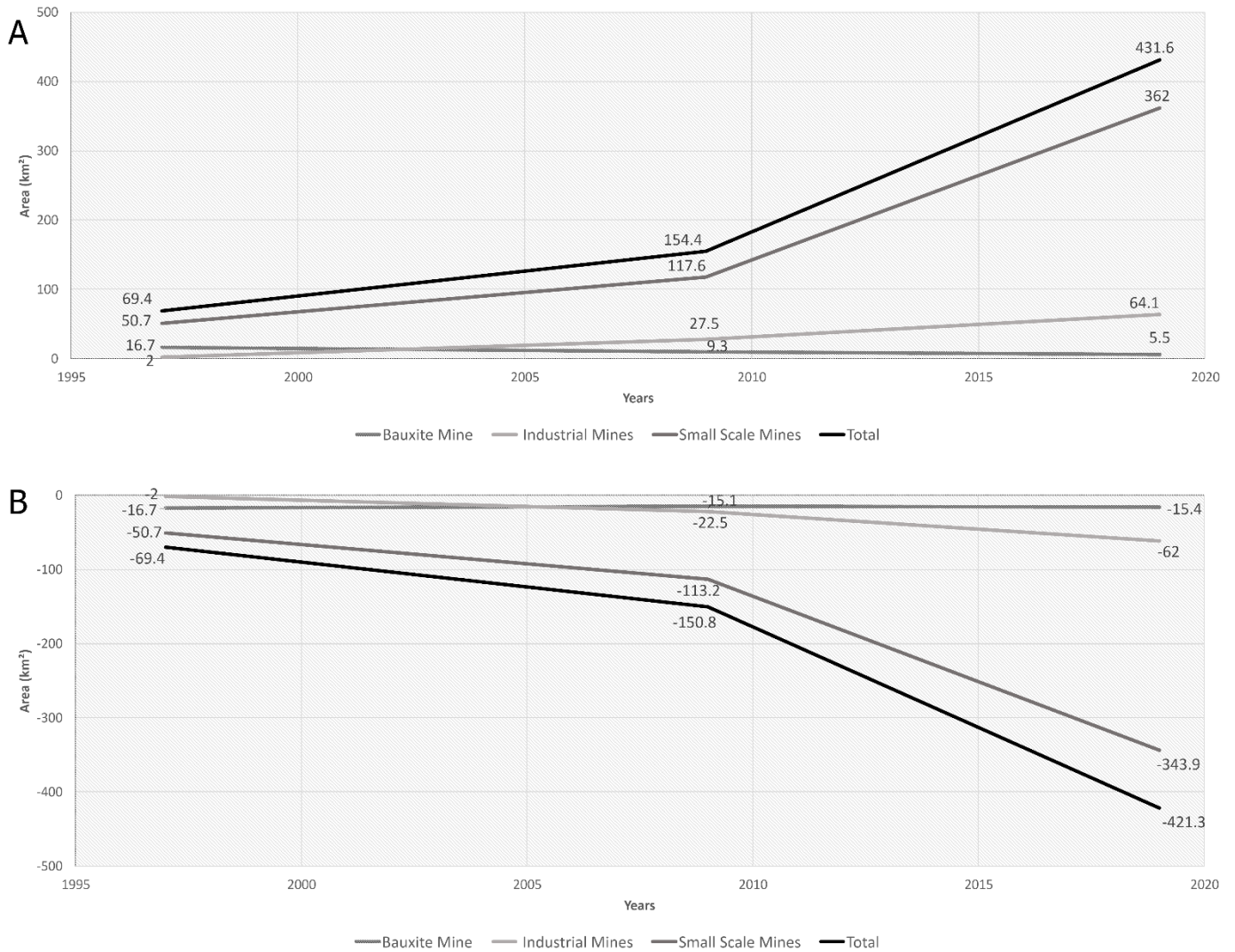
Figure 14: Mining expansion (A) and associated forest loss (B) for bauxite, industrial, small scale (ASGM) and total mines.

The overall trend of mining growth for industrial and small scale gold mining as well as the bauxite mine is displayed in figure 14. Overall, mining grew by 362.2 km² from 69.4 km² in 1997 to 431.6 km² in 2019, an increase of over 522% over 22 years. 77% of this overall growth occurred in the second time period between 2009-2019 compared to 23% for the first time period (1997-2009). The results highlight a clear and alarming pattern of considerable artisanal mining growth in the second time period. Overall, 98% of mining expansion occurred in forested areas (figure 15), leading directly to 351.9 km² of forest loss. The remaining 10.3 km² of mining expansion occurred in either bare soil or urban areas.
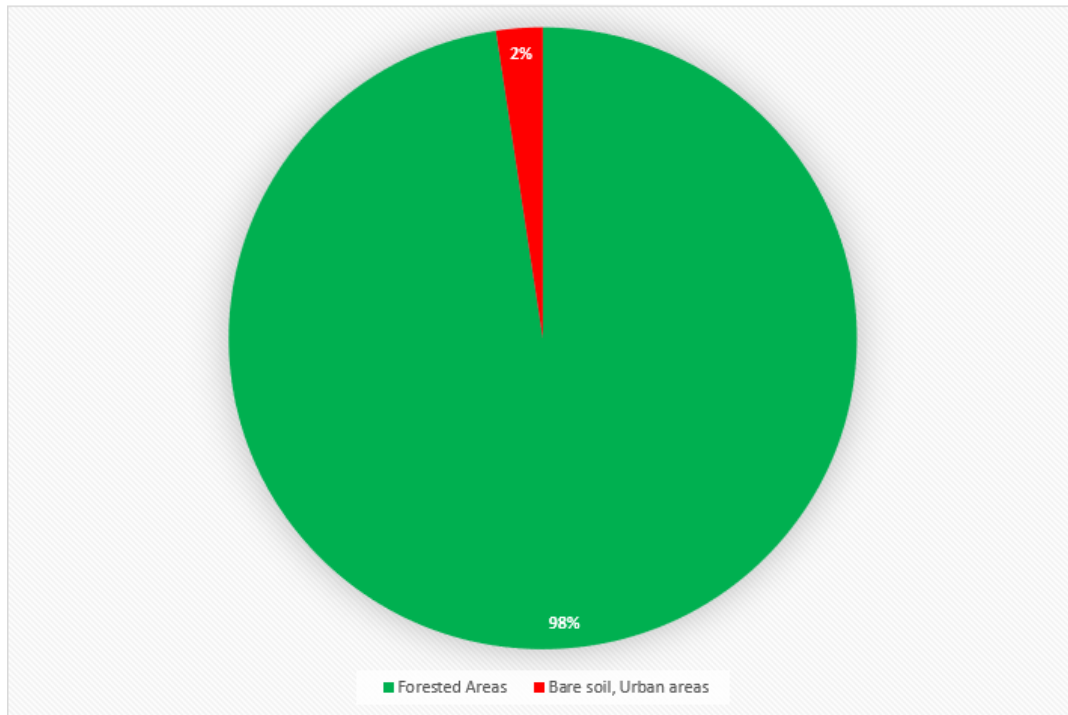
Figure 15: Pie Chart highlighting the percentage of mining expansion into forested areas.

Table 4: Forest Loss and Regrowth for Industrial and Artisanal Mines between 1997 and 2019

	1997 - 2009	2009 - 2019	Total (1997 – 2019)
Industrial Mine Regrowth (km^2)	0.9	1.2	2.1
Industrial Mine Forest Loss (km^2)	-21.4	-40.7	- 62.1
Industrial Mine Net Forest Loss (Regrowth – Forest Loss) (km^2)	**-20.5**	**-39.5**	**-60**
ASGM Regrowth (km^2)	24.9	41.2	66.1
ASGM Forest Loss (km^2)	-87.3	-271.9	-359.2
ASGM Net Forest Loss (Regrowth – Forest Loss) (km^2)	**-62.4**	**-230.7**	**-293.1**

The net forest loss caused directly by both industrial and artisanal mining in both time periods is quantified in table 4. Net forest loss is equal to regrowth minus forest loss. Artisanal mining caused the overwhelming majority of net forest loss (293.1 km^2), accounting for 83% of all net forest loss. Industrial mining on the other hand was responsible for 17% of net forest loss (60 km^2).
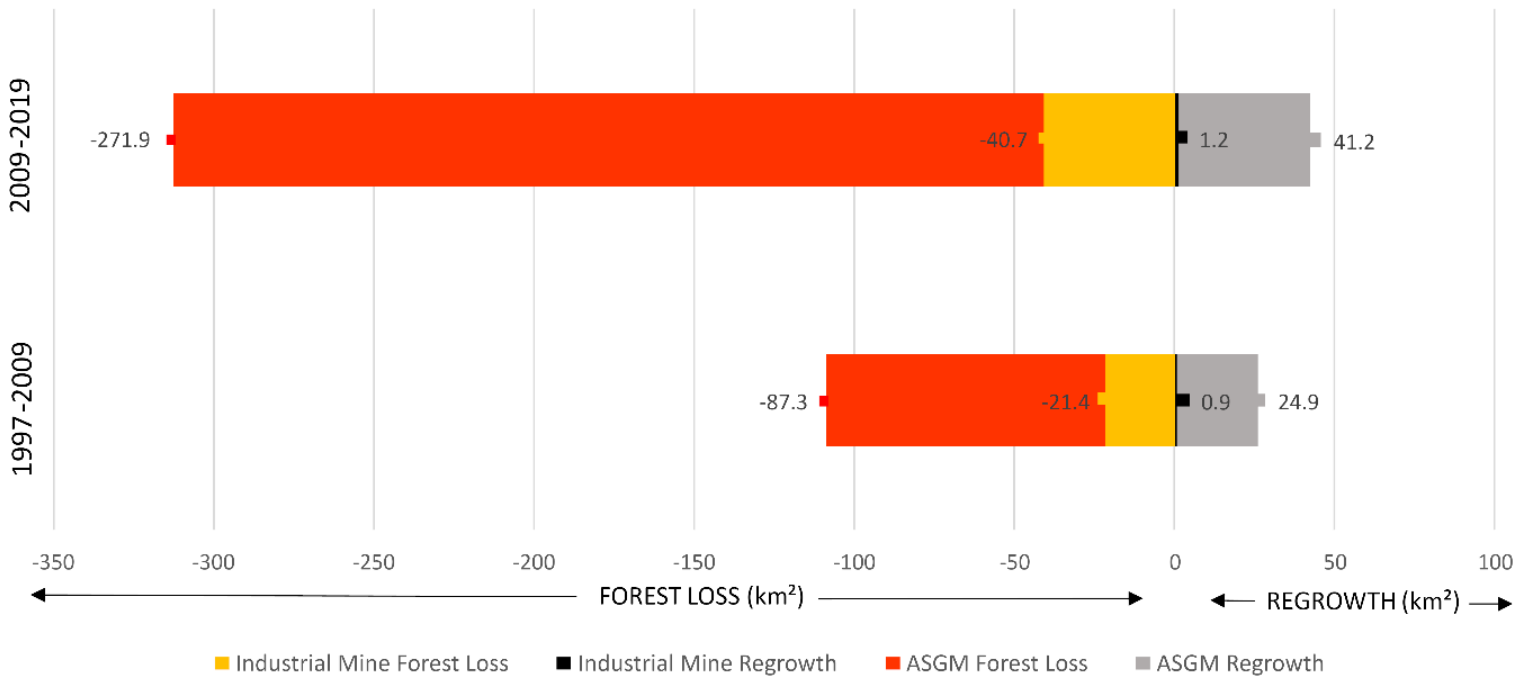

Figure 16: Forest loss and regrowth of forest on abandoned mines in each of the two time periods.

Figure 16 highlights the trend in forest loss and regrowth in more detail. The results indicate that there is a clear continued pattern of overwhelming forest loss in the second time period. Forest loss for both industrial and artisanal mines more than tripled in the second time period compared to the first. This loss of forest cover between 2009-2019 can be attributed mainly to artisanal mines, which accounted for 6 times the forest loss when compared to industrial mines in this time period. Also apparent is the large difference in regrowth rates for both types of mining. Regrowth refers

to abandoned mines where the forest managed to recover and regrow after the mine was abandoned. Regrowth on abandoned mines was 31x greater in artisanal mines compared to industrial. In industrial mines, the ratio of regrowth on abandoned mines compared to forest loss was only 3%, compared to 16% in artisanal mines (Figures 17, 18). This much greater regrowth rate on abandoned mines highlights the dynamic, shifting nature of artisanal mines where exiting mines are frequently abandoned in favour of new locations . This is in stark contrast to the concentrated, static nature of industrial mines, where the area within the mining lease is fully exhausted, leaving little to no abandoned areas and relatively little regrowth.
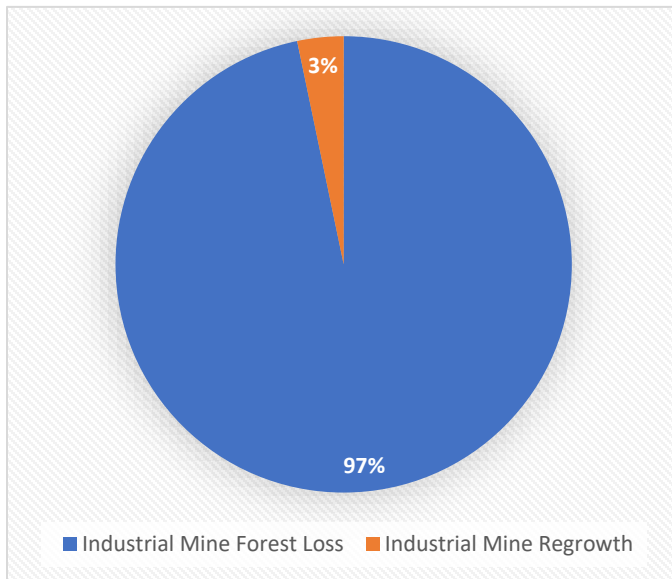

Figure 17: Pie chart showing the ratio of regrowth to forest loss in Industrial mines
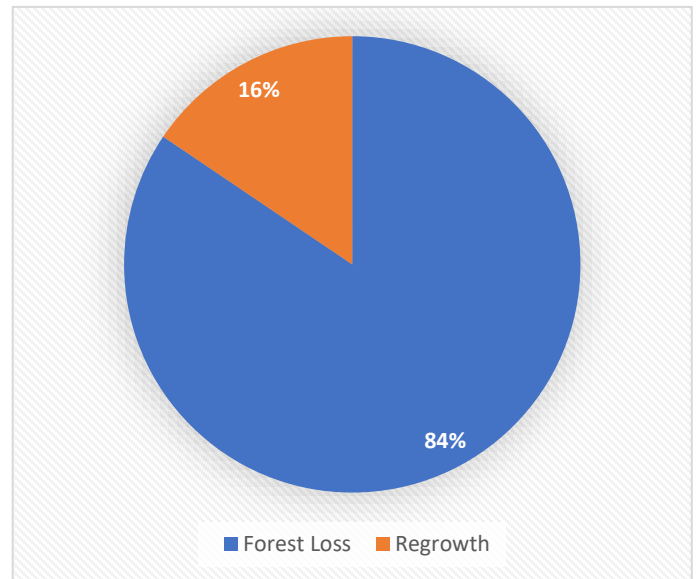
Figure 18: Pie chart showing the ratio of regrowth to forest loss in Artisanal mines.

6.3 FOREST FRAGMENTATION

The differences in the patterns of mining growth become more apparent when a sub-level comparison of industrial and artisanal gold mines at a smaller scale is conducted. These sub-areas (Figure 19) have an area of 1000 km², and were chosen as the two regions where the most concentrated industrial and artisanal gold mining activities occurred.
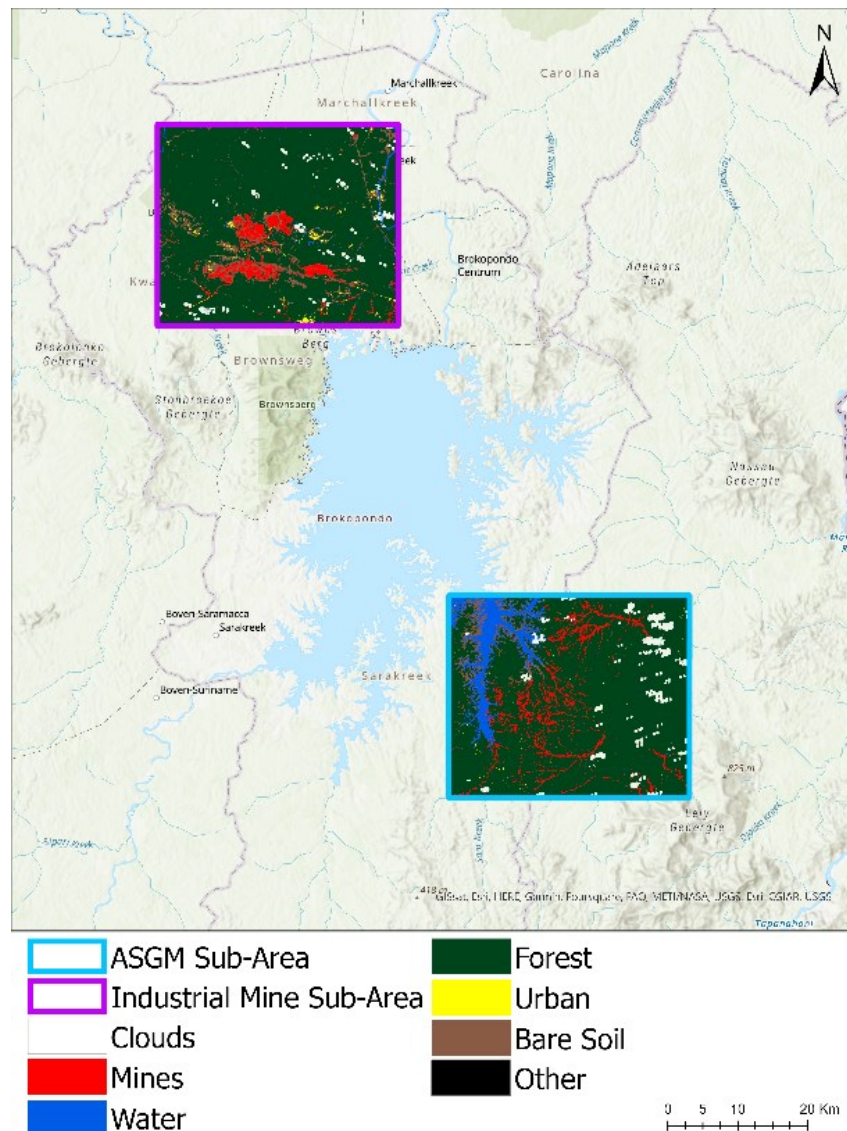

Figure 19: Location of the Sub-Areas

The progression of fragmentation in the two sub-areas is depicted in figure 20. The concentrated nature of industrial mining leads to an earlier onset of fragmentation with the initial construction of large roads that connect different areas of the mine, compared to the relative lack of patch development in the first point in time (2009) for artisanal mining. In 2019, there was a noticeable increase in fragmentation for industrial mining; however, the concentrated nature of mining limited the development of patches to the same geographical area. Conversely, the expansive nature of artisanal mining meant that patch development was less centralised, while the creation of larger patches was also possible as these long, stringy mines began connecting to each other. This caused large, disconnected patches (<20 km²) to be created *between* different mines, rather than the relatively smaller patches (<5 km²) created *within* industrial mines.
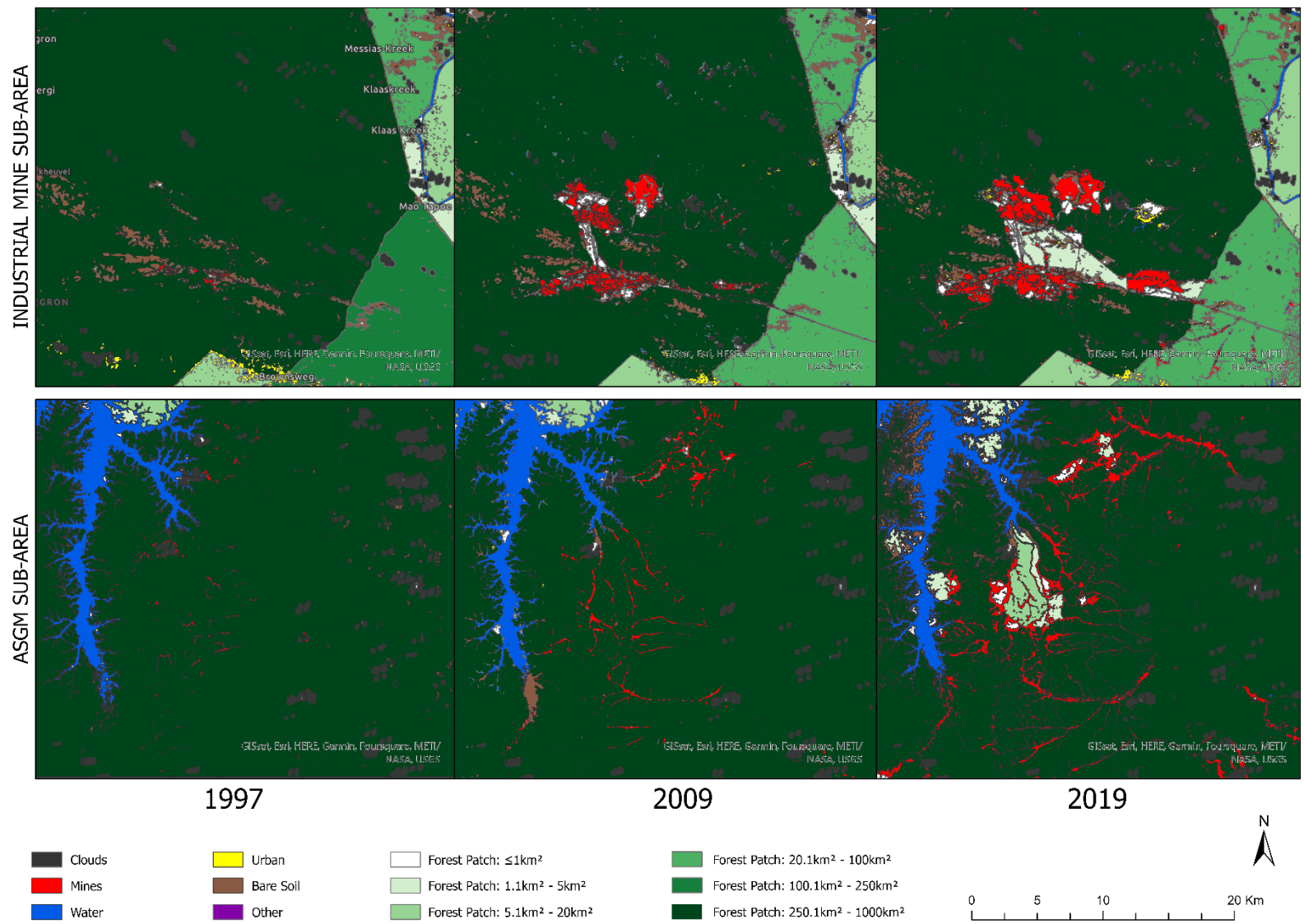
Figure 20: Progression of forest fragmentation (1997-2019) in the two sub-areas

Table 5: Effective mesh size (Meff) of all fragmenting elements including mines, all fragmenting elements excluding mines, and the influence of mines on the Meff (i.e the direct change in the Meff caused by mining, and is calculated as the difference between the first two values)

		1997	2009	2019
INDUSTRIAL MINE AREA	Meff (km²) including mines as a fragmenting element	559.74	493.79	441.6
	Meff (km²) excluding mines as a fragmenting element	561.75	541.2	524.6
	Influence of mining on the Meff (km²)	-2.01 (-0.3%)	-47.41 (-8.8%)	-83.00 (-15.8%)
ASGM AREA	Meff (km²) including mines as a fragmenting element	758.73	719.42	591.52
	Meff (km²) excluding mines as a fragmenting element	765.38	755.35	714.35
	Influence of mining on the Meff (km²)	-6.65 (-0.8%)	-35.93 (-4.8%)	-122.83 (-17.2%)

The pattens of fragmentation seen in figure 20 can be quantified through the fragmentation metric of effective mesh size, which is displayed in table 5 above. The effective mesh size of the entire area, both with mines included as a fragmenting element and with mines excluded, decreased over time in both sub-areas. Once the influence of mines alone was isolated, the results depicted that mines caused a clear decrease in the effective mesh size, and this decrease became larger over time highlighting progressively intensifying fragmentation.

This result is illustrated visually in figure 21. In the first time period, the effective mesh size decreased for both industrial and artisanal mines. While the decrease was greater for industrial mines in the first time period, this was overtaken by artisanal mining in the second time period. These results support the trend seen in the maps, where the concentrated nature of industrial mining caused greater fragmentation in the first time period, but was overtaken by the considerable

increase in fragmentation caused by artisanal mining in the second time period as these mines began connecting to each other.
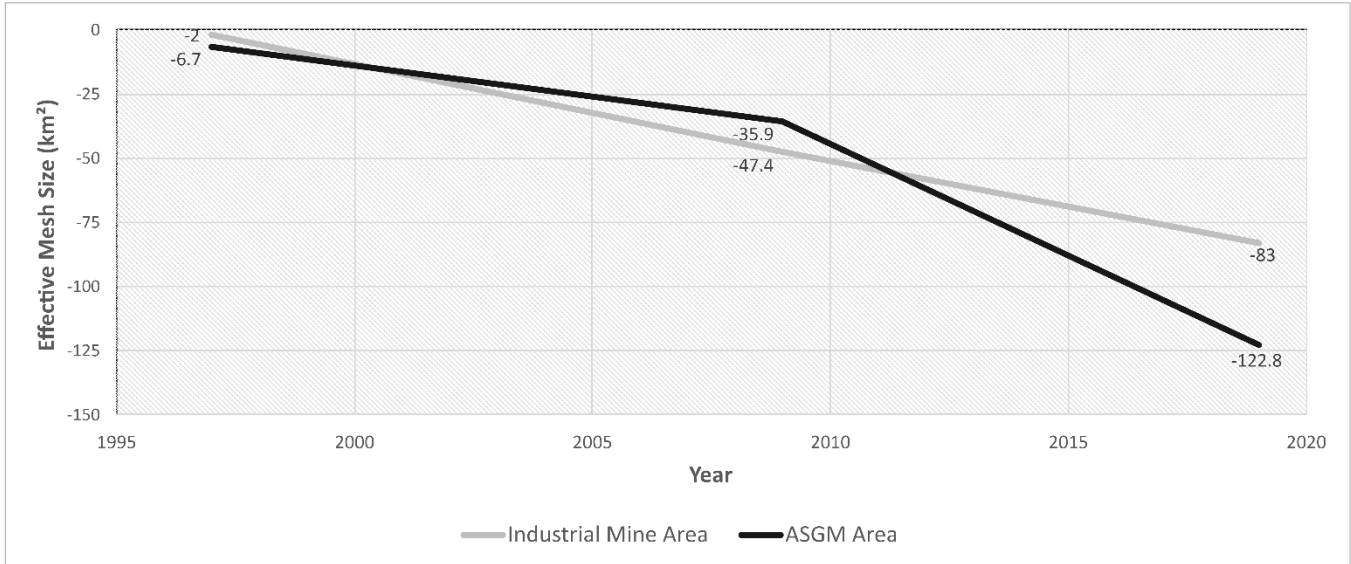

Figure 21: Comparison of decrease in effective mesh size due to mining over time in the two sub-areas

6.4 PHENOLOGY

Further analysis at a sub-level highlighted concerning impacts to the health of the forested ecosystem. The majority of the forested pixels in both the artisanal and industrial mine sub-areas displayed a marked decrease in peak greenness (highlighted in red) in both time periods (figure 22). This is in stark contrast to the positive change in peak greenness (highlighted in green) identified within the majority of forested pixels in the natural, undisturbed sub-area. The overall change from 2001 to 2019 highlights the improvement in forest health over time for the natural area and a simultaneous decline in health for both mining sub-regions. The lack of data or pixels in certain parts of the sub-areas is due to issues with cloud cover, where in these areas data was not made available due to extensive cloud coverage in those areas for that year.

ASGM SUB-AREA

INDUSTRIAL SUB-AREA

NATURAL SUB-AREA

2001 to 2009   2009 to 2019   2001 to 2019
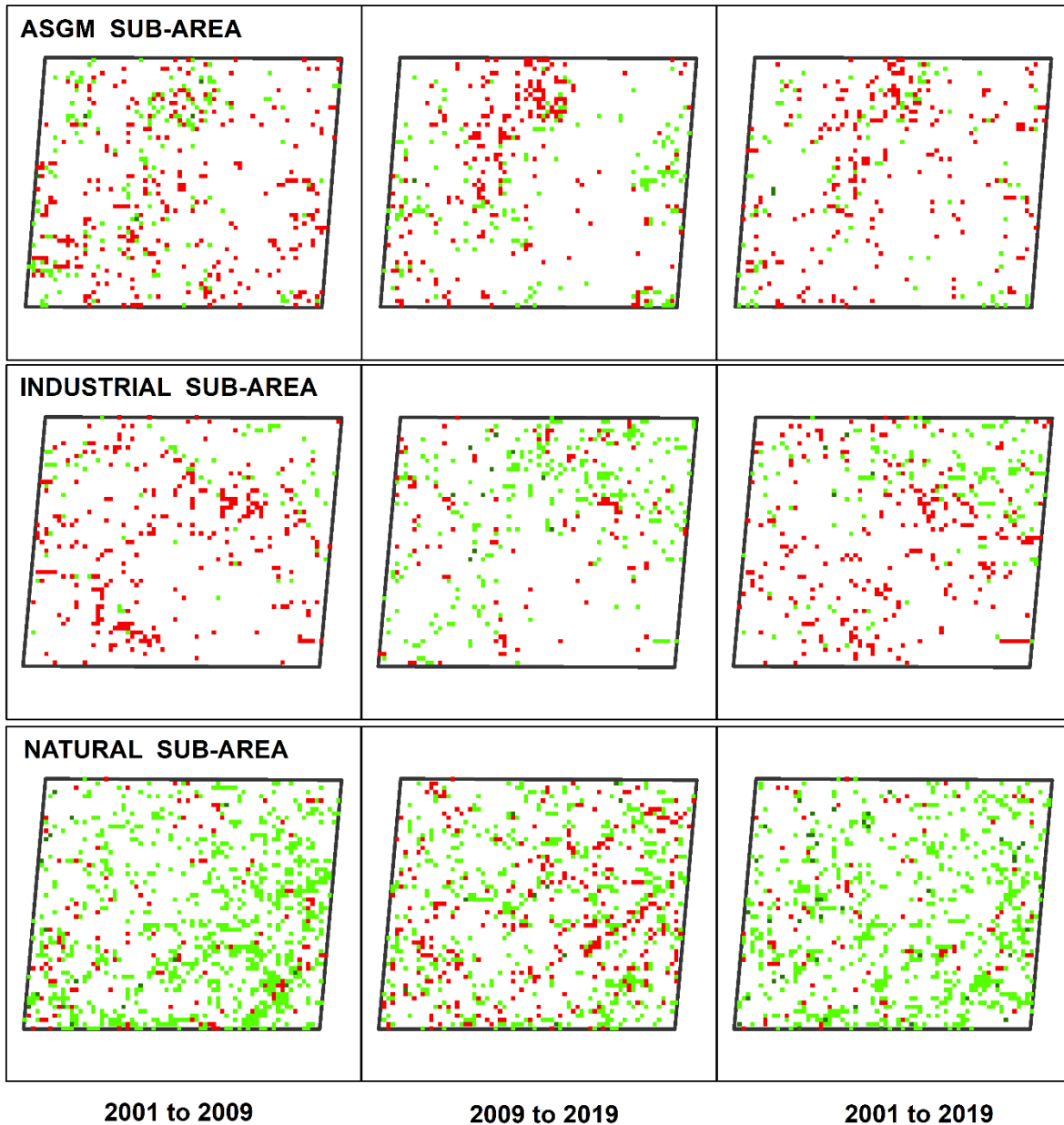
Difference in Peak Greenness: < 0   0 - 1,000   1000+

Figure 22: Change in peak greenness for the two mining sub areas and the natural sub-area. For each time period, change in peak greenness is calculated as the peak greenness value of the second year (e.g. 2009) minus the peak greenness value of the first year (e.g. 2001), for each pixel in the image.

The average peak greenness for the entire study area (Figure 23) underscores this trend of increasing peak greenness over time for the natural area, and gradual decline in peak greenness of the forest in mining regions. The difference between the average peak values (which is a proxy for vegetation health) of the different sites were significant for all site pairs with P-values < 0.05, highlighting that the vegetation health of the natural site was significantly higher than the health of the vegetation for the industrial and ASGM sites. This decline in peak greenness is more pronounced for the artisanal mine sub-area, highlighting the greater impacts this type of mining poses for the health of the surrounding forests. In 2010, there was a marked drop in peak greenness that was consistent across all study areas. This was due to the severe drought in the Amazon Basin in 2010 which brought about drought stress in trees, resulting in abnormally low vegetation index values for that year (Nasa Earth Observatory 2011)
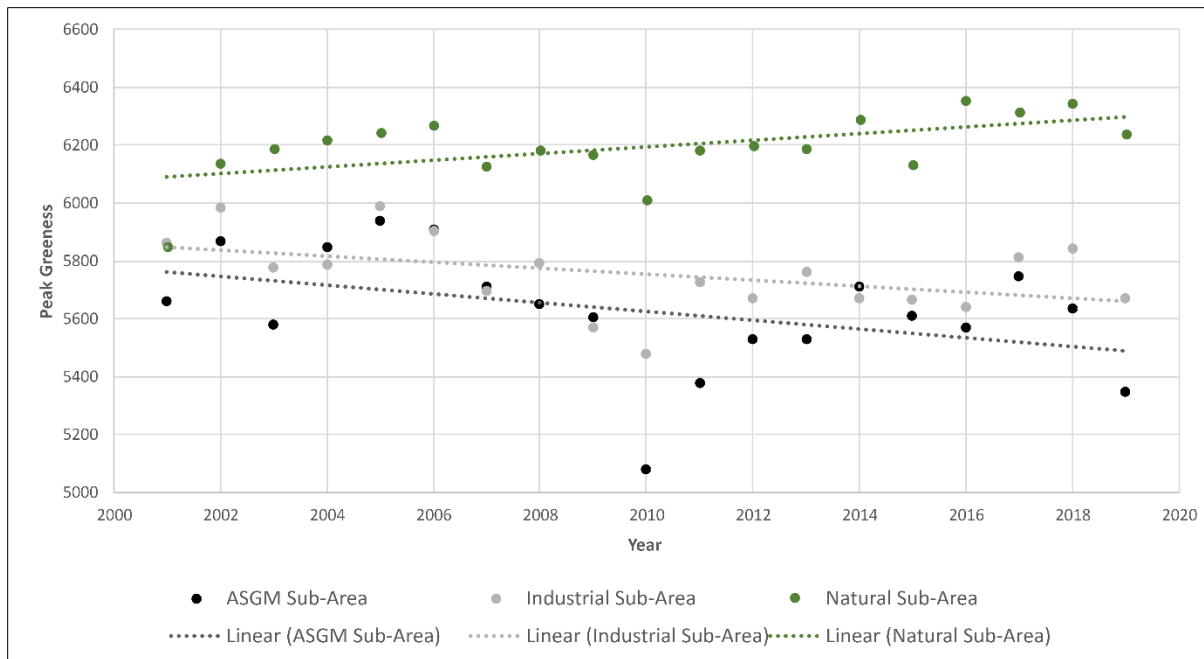

Figure 23: Change in average peak greenness in the three sub-areas over time.

7. DISCUSSION

7.1 – RE-CLASSIFICATION MODEL

The mining detection accuracy of 89.5% (84% producer accuracy, 95% user accuracy) that was achieved by the GEE + Ratio/Threshold Reclassification model approach developed in this study shows the feasibility of this semi-automated cloud processing-based algorithm in producing reliable and highly accurate results for mining detection. Other studies reported varying degrees of success depending on the method. Among the well-established line of CLASLITE methodologies, the most successful approach was that of Asner (2013), who obtained an overall mining accuracy of 92.5% (93% producer accuracy, 92% user accuracy). Using the same approach, Elmes et al. (2014) revealed an accuracy of 70% (71% producer accuracy, 69% user accuracy), while Caballero Espejo (2018), when using CLASLITE alone, recorded an accuracy of 67.5% (80% producer accuracy, 55% user accuracy), which improved to 79.5% (81% producer, 78% user accuracy) once their automated GFC-fusion re-classification approach was applied. In the first attempt at cloud processing for mining detection, Lobo et al. (2018) recorded an accuracy of 74.5% (80% producer accuracy, 69% user accuracy). Despite the speed at which cloud processing can classify images, Lobo et al. (2018) relied heavily on manual reclassification to improve the final accuracy, much like Asner (2013) and Elmes (2014) with the CLASLITE approach. On the other hand, the automated approach developed by Caballero Espejo (2018) still relied on downloading and subsequent offline image processing, which significantly slows down the classification process compared to cloud processing, which can process images that take hours when using traditional software in a matter of seconds to minutes (Lobo et al. 2018).

For the future of mining detection, the cloud processing approach is clearly advantageous, but can only be unlocked to its full potential when combined with automated re-classification, otherwise the gains in faster processing times are lost with the extensive step of manual reclassification. This study is therefore proposing a pioneer method that leverages on-the-cloud machine learning with semi-automated reclassification to ensure rapid and highly accurate mining detection. As the first documented method to integrate both cloud processing and an semi-automated re-classification model, this approach combines the advantages of the previous methods while also addressing their

shortcomings. The 89.5% accuracy achieved by the model compares favourably to the two most advanced recent methods by Caballero Espejo et al. (2018) and their CLASLITE + GFC Fusion method (79.5% accuracy), and by Lobo et al. (2018) and their cloud processing + manual reclassification approach (74.5% accuracy). This highlights that the advantage of speed gained by this proposed method is also coupled with highly accurate and reliable detection.

For small study areas the use of spectral unmixing by Asner (2013) remains the most accurate and reliable form of mining detection with a 92.5% mining accuracy; however, the lack of both automation and cloud processing means that this approach is not easily transferable to very large study areas due to the length of time the processing and manual reclassification steps would take. The speed and accuracy of the GEE+ semi-automated reclassification approach proposed in this study ensures that it is a more suitable option for large study areas.

Additionally, the model also addresses another notable gap in the previous methodologies, as it is the first to be tested in an urban setting. With other methods opting for various combinations of mining, water, agriculture, forest, and clear-cut land as LULC classes, there is a noticeable absence of an urban class. The high spatial diversity and spectral variability of urban areas imply that these areas are notoriously tricky to classify (Mitraka et al. 2016), and when coupled with the similarly high spectral variability of mining regions, creates a cocktail that results in frequent misclassifications between the two classes. While the spectral unmixing algorithms used by previous studies have proved useful in classifying urban areas (Mitraka et al. 2016), their performance in accurately distinguishing between mines and urban areas is yet to be determined. The proposed method in this paper, in contrast, is capable of classifying mines in a highly urbanised setting, which may prove necessary in the future as urban growth and projected mining expansion will increase the possibilities of more frequent intersections between these two classes.

Another advantage of the model is the flexibility of its design. As a reclassification model designed to identify patterns in the spatial distribution of pixels post classification, there is a potential for it to be combined with different classification algorithms. For example, spectral unmixing can be used instead of the CART algorithm for the initial classification which is then used as an input to the model. The model's flexibility also allows it to be deconstructed for other uses, as its ability to reclassify misclassified mining pixels in urban areas (improving the urban accuracy by 14 percentage points) highlights its ability to be used as a standalone urban reclassification model.

The mining class can theoretically be swapped with another to reclassify the occurrence of those pixels in urban areas. This step would require some knowledge of the spatial patterns exhibited by the pixels of the other class post classification, along with some adjustment of the parameters. The urban reclassification portion of the model can also be removed if mining detection in remote areas is desired where an urban class doesn't exist.

Despite its many advantages, the model exhibited a tendency to overclassify mining. While accurately identifying and reclassifying pixels within mines and cities/towns, the presence of misclassified mining and urban pixels located adjacent to each other in other areas caused misattribution of these areas to either the mining or urban class. This was seen with sediment deposits on the shore of the lake which were misclassified as mines due to the mix of misclassified mine-urban pixels in this area. While this misclassification implied that the presence of a manual reclassification step was necessary to identify and remove overclassified areas, this step was very short as the overclassified areas were all sediment deposits located in one area on the banks of the lake, making them easily identifiable. In mining studies, the reclassification of overclassified areas is a faster and more efficient process than the issue of under classification faced by previous studies Asner et al. (2013), Elmes et al. (2014) and Lobo et al. (2018). Under-classification requires an extensive manual reclassification step to verify all mining regions and assign missed areas to the mining class. Semi-automated reclassification models such as the one proposed in this study, ensure that under classification of mining regions are eliminated in a highly accurate manner (89.5% accuracy of mining regions), implying that manual reclassification only needs to be done on large, easily identifiable areas of overclassification, such as the area of sediment deposits on the banks of the lake. Future research can improve this limitation of the model, by potentially creating a new class to identify and split sediment deposits from the mining and urban class, or through the use of a different classification algorithm which performs better in identifying sediment deposits as a separate class. The performance of the reclassification model is therefore inherently dependent on the accuracy of the initial classification, and through improvements in the performance of the initial classification, the re-classification model will perform even better. Alternatively, the manual reclassification of the lake shoreline sediments could be included in the automated reclassification model by buffering the lake areas and removing the buffered lake areas from the classified map.

While the method proposed in this paper has its limitations, it succeeds in providing a technologically advanced framework for mining detection in a highly adaptable and flexible format, providing significant potential for further research to combine this method with other, potentially more suitable classification algorithms than CART and improve it even further.

7.2 MINING GROWTH, FOREST FRAGMENTATION AND PHENOLOGY

Overall, the results all show a strong trend of artisanal mining causing more forest loss, leading to more fragmentation over time, and causing greater impacts on the health of the forested ecosystem. These impacts were all greater in the second time period (2009-2019). This can be attributed to the 2008 global financial crisis which caused a 12.8% increase in gold prices the following year (Hergt 2013). This increase intensified well after the recession due to the role of gold as an economic stabilizer in extreme market conditions (Aruga and Kannan 2020). This increase in prices likely served as an incentive for increased mining exploration. This is corroborated by Asner (2013), who found that the annual rate of mining expansion in Peru tripled following 2008, while Caballero Espejo et al. (2018) also noted that in 2010, gold mining in Peru increased 3x the previous level. The forest loss associated with this growth highlighted an interesting pattern for artisanal mining, where regrowth on abandoned areas was 31x greater than for industrial mines. This finding demonstrates the dynamic nature of artisanal mines, which is due to the fact that miners "have been known to move up and down rivers at a high temporal frequency" (Asner 2013), routinely changing locations and abandoning former mines.

In addition to forest loss, the growth of mining led to different patterns of forest fragmentation for artisanal and industrial mining. The concentrated, centralised pattern of fragmentation displayed by industrial mines can be attributed to the spatial restrictions imposed by mining concessions, where the government limits mining to a specific ore within a confined area (Perez 1970). Artisanal mining, in contrast, is often conducted without the authorisation by the government and is therefore not subjected to spatial constraints, enabling a more expansive pattern of growth and a less centralised pattern of fragmentation. Fragmentation for artisanal mining was caused by adjacent

mining regions connecting to each other, while the fragmentation caused by industrial mining was associated with the development of large road networks within the mine. This pattern was also noticed by Siqueria-Gray et al. (2020), who found that fragmentation due to mining occurs particularly through the establishment of secondary infrastructure to transport and process extracted materials. This separation and isolation of patches caused by mining induced fragmentation causes a multitude of impacts to biodiversity. According to Kumi et al. (2021), fragmentation makes the dispersal of native species from one patch to another more difficult and places harsh constraints on plant species near the edge of fragments, subsequently leading to elevated levels of plant species mortality and a reduction of plant species diversity. The creation of smaller fragments of forest caused by mining also impacts larger Amazonian fauna. According to Laurance et al. (2018), patches in the Amazon rainforest of less than 1 km² in size are unable to support viable populations of primates and larger herbivorous mammals. Additionally, smaller fragments also display elevated rates of species loss compared to larger fragments (Laurance et al. 2018).

In addition to these impacts, the results highlighted a clear decrease in the health of the forest, particularly for ASGM areas. The more pronounced decrease in peak greenness and vegetation health for ASGM can be attributed in large part due to the illegal use of mercury in these mines, which leaches into the surrounding soils and waterways near mines. According to Gworek et al. (2020) out of all industrial emissions sources (factories, highways, smelters, etc) the highest soil mercury levels are consistently found near mining sites which use this chemical. This accumulation of mercury in the soil can have a toxic effect on trees, causing growth retardation even at low concentrations (Gworek et al. 2020). The sustained and consistent use of these chemicals near ASGM sites would therefore explain the difference in peak greenness and vegetation health between the ASGM and industrial mining sites. In contrast to this decrease, the natural sub-area which was used as a control, displayed a gradual increase in peak greenness. This can be attributed to the geography of the natural sub-area, as it was located in the Central Suriname Nature Reserve. In their study on the conservation efficiency of nature reserves on the Tibetan Plateau, Hua et al. (2022), found that nature reserves had a positive influence on vegetation greenness, cover and productivity, with over 40% of the study areas in nature reserves displaying a positive impact on vegetation growth. This could explain the increase in peak greenness found in the natural sub-area under undisturbed conditions. The significant difference (P-values <0.05)

found by this study between the increasing peak greenness in the natural site compared to the decreasing peak greenness for the ASGM and industrial mining sites highlights just how greatly mining (and likely the use of mercury in ASGM mines) impacts the health of the surrounding forest. This has potentially far-reaching implications on the global climate by affecting carbon fluxes in the Amazon, as a study by Asner et al. (2013) emphasized that ASGM induced forest degradation contributed greatly to carbon storage loss in the Peruvian Amazon.

Overall, the negative impacts of mining are widespread and alarming, and the trend of remarkable mining growth after the global recession and gold price surge in 2008 is even more alarming when considering the additional 25% increase in gold prices in 2020 caused by the most recent global crisis, the COVID 19 pandemic (Galbraith and Kalamandeen 2020). Recent trends therefore show that future mining expansion is likely to continue, and would require a monumental effort at the policy level to abate the potentially catastrophic future environmental impacts.

8. CONCLUSION

The objectives of this study were to analyse and quantify the progression of mining in Suriname over the last 2 decades, and how this has in turn impacted the health (phenology) and structure (fragmentation) of the forest. The study also improved existing classification techniques and developed a new method to classify mines utilising both cloud processing with Google Earth Engine and a semi-automated reclassification model. This was achieved with the proposed pioneer method that resulted in final mine maps with average overall accuracies of 89.5% (84% producer accuracy, 95% user accuracy). The approach outperformed many of the currently available methods used for mining detection, providing a technologically advanced approach, which highlights that speed and efficiency in mining detection can be coupled with reliable and highly accurate results. The results of the classification method highlighted that mining increased by 362.2 km² from 69.4 km² in 1997 to 431.6 km² in 2019, an increase by over 522% over 22 years. Most of this growth (77%) came in the second time period between 2009 and 2019 and was dominated by a massive increase in artisanal mining. This growth led directly to 351.9km² of forest loss, 83% of which was due to artisanal mining. The results of the fragmentation analysis highlighted a similar story: While the concentrated nature of industrial mining may have caused greater fragmentation in the first time period, it was overtaken by the considerable increase in fragmentation caused by artisanal mining in the second time period as these mines began to connect to each other. Between 1997-2019, the effective mesh size decreased by 122.8 km² for the artisanal mine sub-area, compared to a decrease of 83 km² for the industrial mine sub-area. The results of the phenology study highlighted that mining in Suriname has led to a decline in the health of the surrounding forested ecosystem, and this decline was more pronounced for the artisanal mine sub-area, underscoring the clear trend of greater growth, more forest loss, greater fragmentation, and greater decline in the health of the forest from artisanal mining compared to industrial mining.

In quantifying the growth of mining and assessing its impacts on the health and structure of the forest, this study has achieved its objectives. However, there are some limitations within the methods that can be further studied and improved upon in further research.

Firstly, this analysis is limited by the spatial resolution of the imagery, which is 30 m x 30 m. This means that changes or objects of interest smaller than 30 m x 30 m will not be identified. Future research should look into Sentinel data or the image fusion of Landsat panchromatic bands and multispectral bands. Secondly, cloud cover is a serious problem in the Amazon region, limiting the availability of data for continuous assessment and monitoring. Future research should explore the incorporation of microwave data such as Sentinel 1 into classification algorithms. Additionally, the use of a texture analysis to help distinguish mining regions from other classes, as well as exploring the possibility of image segmentation or object based classification for the identification of water bodies within mines, should be explored in future research as a way of improving the accuracy of mining detection. Lastly, the issue of overclassification with the areas of sediment deposits on the edge of the lake could be solved by incorporating a buffer around the lake and excluding all areas within a certain distance of the lake from the re-classification model. This would further reduce the manual reclassification step, bringing the model even closer to full automation.

9. BIBLIOGRAPHY

Ahlström, Anders, Paul A Miller, and Benjamin Smith. 2012. "Too Early to Infer a Global NPP Decline since 2000." *Geophysical Research Letters*, 6.

Albert, James S., Tiago P. Carvalho, Paulo Petry, Meghan A. Holder, Emmanuel L. Maxime, Jessica Espino, Isabel Corahua, et al.. 2011. "Aquatic Biodiversity in the Amazon: Habitat Specialization and Geographic Isolation Promote Species Richness." *Animals* 1 (2): 205–41. https://doi.org/10.3390/ani1020205.

Almeida-Filho, R. 2002. "Digital Processing of a Landsat-TM Time Series for Mapping and Monitoring Degraded Areas Caused by Independent Gold Miners, Roraima State, Brazilian Amazon." *Remote Sensing of Environment* 79 (1): 42–50. https://doi.org/10.1016/S0034-4257(01)00237-1.

"Amazon Gold Rush: Gold Mining in Suriname." 2022. 2022. https://www.amazonteam.org/maps/suriname-gold/.

Aruga, Kentaka, and Sudha Kannan. 2020. "Effects of the 2008 Financial Crisis on the Linkages among the Oil, Gold, and Platinum Markets." Edited by David McMillan. *Cogent Economics & Finance* 8 (1): 1807684. https://doi.org/10.1080/23322039.2020.1807684.

Asner, G. P. 2005. "Selective Logging in the Brazilian Amazon." *Science* 310 (5747): 480–82. https://doi.org/10.1126/science.1118051.

Asner, G. P., W. Llactayo, R. Tupayachi, and E. R. Luna. 2013. "Elevated Rates of Gold Mining in the Amazon Revealed through High-Resolution Monitoring." *Proceedings of the National Academy of Sciences* 110 (46): 18454–59. https://doi.org/10.1073/pnas.1318271110.

Asner, Gregory P, and Raul Tupayachi. 2016. "Accelerated Losses of Protected Forests from Gold Mining in the Peruvian Amazon." *Environmental Research Letters* 12 (9): 094004. https://doi.org/10.1088/1748-9326/aa7dab.

Barbosa, Luiz C. 2000. *The Brazilian Amazon Rainforest: Global Ecopolitics, Development, and Democracy*. University Press of America.

Barona, Elizabeth, Navin Ramankutty, Glenn Hyman, and Oliver T Coomes. 2010. "The Role of Pasture and Soybean in Deforestation of the Brazilian Amazon." *Environmental Research Letters* 5 (2): 024002. https://doi.org/10.1088/1748-9326/5/2/024002.

Batar, Amit, Teiji Watanabe, and Ajay Kumar. 2017. "Assessment of Land-Use/Land-Cover Change and Forest Fragmentation in the Garhwal Himalayan Region of India." *Environments* 4 (2): 34. https://doi.org/10.3390/environments4020034.

Boucher, Doug, and Dora Chi. 2018. "Amazon Deforestation in Brazil: What Has Not Happened and How the Global Media Covered It." *Tropical Conservation Science* 11 (January): 194008291879432. https://doi.org/10.1177/1940082918794325.

Boucher, Doug, Sarah Roquemore, and Estrellita Fitzhugh. 2013. "Brazil's Success in Reducing Deforestation." *Tropical Conservation Science* 6 (3): 426–45. https://doi.org/10.1177/194008291300600308.

Caballero Espejo, Jorge, Max Messinger, Francisco Román-Dañobeytia, Cesar Ascorra, Luis Fernandez, and Miles Silman. 2018. "Deforestation and Forest Degradation Due to Gold Mining in the Peruvian Amazon: A 34-Year Perspective." *Remote Sensing* 10 (12): 1903. https://doi.org/10.3390/rs10121903.

Cardoso, Domingos, Tiina Sarkinen, Sara Alexander, Andre M. Amorim, Volker Bittrich, Marcela Celis, Douglas C. Daly, et al.. 2017. "Amazon Plant Diversity Revealed by a Taxonomically Verified Species List." *Proceedings of the National Academy of Sciences of the United States of America* 114 (40): 10695–700. https://doi.org/10.1073/pnas.1706756114.

Castello, Leandro, and Marcia N. Macedo. 2016. "Large-Scale Degradation of Amazonian Freshwater Ecosystems." *Global Change Biology* 22 (3): 990–1007. https://doi.org/10.1111/gcb.13173.

Chakraborty, Anusheema, Aniruddha Ghosh, Kamna Sachdeva, and P.K. Joshi. 2017. "Characterizing Fragmentation Trends of the Himalayan Forests in the Kumaon Region of Uttarakhand, India." *Ecological Informatics* 38 (March): 95–109. https://doi.org/10.1016/j.ecoinf.2016.12.006.

Charou, E., M. Stefouli, D. Dimitrakopoulos, E. Vasiliou, and O. D. Mavrantza. 2010. "Using Remote Sensing to Assess Impact of Mining Activities on Land and Water Resources." *Mine Water and the Environment* 29 (1): 45–52. https://doi.org/10.1007/s10230-010-0098-0.

Clay, Elizabeth, Rafael Moreno-Sanchez, Juan Torres-Rojo, and Francisco Moreno-Sanchez. 2016.
“National Assessment of the Fragmentation Levels and Fragmentation-Class Transitions of the
Forests in Mexico for 2002, 2008 and 2013.” *Forests* 7 (3): 48. https://doi.org/10.3390/f7030048.

Elmes, Arthur, Josué Gabriel Yarlequé Ipanaqué, John Rogan, Nicholas Cuba, and Anthony
Bebbington. 2014. “Mapping Licit and Illicit Mining Activity in the Madre de Dios Region of
Peru.” *Remote Sensing Letters* 5 (10): 882–91. https://doi.org/10.1080/2150704X.2014.973080.

Fagiewicz, Katarzyna. 2014. “Spatial Processes of Landscape Transformation in Mining Areas (Case
Study of Opencast Lignite Mines in Morzysław, Niesłusz, Gosławice),” 15.

Farda, N. M. 2017. “Multi-Temporal Land Use Mapping of Coastal Wetlands Area Using Machine
Learning in Google Earth Engine.” *IOP Conference Series: Earth and Environmental Science* 98
(December): 012042. https://doi.org/10.1088/1755-1315/98/1/012042.

Fehlenberg, Verena, Matthias Baumann, Nestor Ignacio Gasparri, Maria Piquer-Rodriguez, Gregorio
Gavier-Pizarro, and Tobias Kuemmerle. 2017. “The Role of Soybean Production as an
Underlying Driver of Deforestation in the South American Chaco.” *Global Environmental
Change* 45 (July): 24–34. https://doi.org/10.1016/j.gloenvcha.2017.05.001.

Friedl, Mark, Gray, Josh, and Sulla-Menashe, Damien. 2019. “MCD12Q2 MODIS/Terra+Aqua
Land Cover Dynamics Yearly L3 Global 500m SIN Grid V006.” NASA EOSDIS Land
Processes DAAC. https://doi.org/10.5067/MODIS/MCD12Q2.006.

Galbraith, David, and Michelle Kalamandeen. 2020. “Gold Mining Leaves Deforested Amazon Land
Barren for Years, Find Scientists.” The Conversation. 2020. http://theconversation.com/gold-
mining-leaves-deforested-amazon-land-barren-for-years-find-scientists-141639.

Girardin, Cécile A. J., Yadvinder Malhi, Christopher E. Doughty, Daniel B. Metcalfe, Patrick Meir,
Jhon del Aguila-Pasquel, Alejandro Araujo-Murakami, et al.. 2016. “Seasonal Trends of
Amazonian Rainforest Phenology, Net Primary Productivity, and Carbon Allocation: Seasonal
Trends of Amazonian Forests.” *Global Biogeochemical Cycles* 30 (5): 700–715.
https://doi.org/10.1002/2015GB005270.

Girvetz, Evan H., James H. Thorne, Alison M. Berry, and Jochen A.G. Jaeger. 2008. “Integration of
Landscape Fragmentation Analysis into Regional Planning: A Statewide Multi-Scale Case Study

from California, USA." *Landscape and Urban Planning* 86 (3–4): 205–18. https://doi.org/10.1016/j.landurbplan.2008.02.007.

Gorelick, Noel, Matt Hancher, Mike Dixon, Simon Ilyushchenko, David Thau, and Rebecca Moore. 2017. "Google Earth Engine: Planetary-Scale Geospatial Analysis for Everyone." *Remote Sensing of Environment* 202 (December): 18–27. https://doi.org/10.1016/j.rse.2017.06.031.

Gworek, Barbara, Wojciech Dmuchowski, and Aneta H. Baczewska-Dąbrowska. 2020. "Mercury in the Terrestrial Environment: A Review." *Environmental Sciences Europe* 32 (1): 128. https://doi.org/10.1186/s12302-020-00401-x.

Hacon, Sandra de Souza, Marcelo Oliveira-da-Costa, Cecile de Souza Gama, Renata Ferreira, Paulo Cesar Basta, Ana Schramm, and Decio Yokota. 2020. "Mercury Exposure through Fish Consumption in Traditional Communities in the Brazilian Northern Amazon." *International Journal of Environmental Research and Public Health* 17 (15): 5269. https://doi.org/10.3390/ijerph17155269.

Hargrave, Jorge, and Krisztina Kis-Katos. 2013. "Economic Causes of Deforestation in the Brazilian Amazon: A Panel Data Analysis for the 2000s." *Environmental & Resource Economics* 54 (4): 471–94. https://doi.org/10.1007/s10640-012-9610-2.

Heemskerk, Marieke. 2002. "Livelihood Decision Making and Environmental Degradation: Small-Scale Gold Mining in the Suriname Amazon." *Society & Natural Resources* 15 (4): 327–44. https://doi.org/10.1080/089419202753570819.

Hentschel, Thomas, Felix Hruschka, Michael Priester, and Projekt-Consult GmbH. 2002. "Global Report on Artisanal & Small-Scale Mining," January, 67.

Hergt, Brian. 2013. "Gold Prices during and after the Great Recession," 8.

Hua, Ting, Wenwu Zhao, Francesco Cherubini, Xiangping Hu, and Paulo Pereira. 2022. "Effectiveness of Protected Areas Edges on Vegetation Greenness, Cover and Productivity on the Tibetan Plateau, China." *Landscape and Urban Planning* 224 (August): 104421. https://doi.org/10.1016/j.landurbplan.2022.104421.

Jaeger, Jochen A G. 2000. "Landscape Division, Splitting Index, and Effective Mesh Size: New Measures of Landscape Fragmentation."

Jaeger, Jochen, Rene Bertiller, and Christian Schwick. 2007. "Degree of Landscape Fragmentation in Switzerland: Quantitative Analysis 1885–2002 and Implications for Traffic Planning and Regional Planning."

Jaeger, Jochen A.G., René Bertiller, Christian Schwick, Kalin Müller, Charlotte Steinmeier, Klaus C. Ewald, and Jaboury Ghazoul. 2008. "Implementing Landscape Fragmentation as an Indicator in the Swiss Monitoring System of Sustainable Development (Monet)." *Journal of Environmental Management* 88 (4): 737–51. https://doi.org/10.1016/j.jenvman.2007.03.043.

Kemp, D., and J.R. Owen. 2019. "Characterising the Interface between Large and Small-Scale Mining." *The Extractive Industries and Society* 6 (4): 1091–1100. https://doi.org/10.1016/j.exis.2019.07.002.

Kim, Yeonjoo, Ryan G. Knox, Marcos Longo, David Medvigy, Lucy R. Hutyra, Elizabeth H. Pyle, Steven C. Wofsy, Rafael L. Bras, and Paul R. Moorcroft. 2012. "Seasonal Carbon Dynamics and Water Fluxes in an Amazon Rainforest." *Global Change Biology* 18 (4): 1322–34. https://doi.org/10.1111/j.1365-2486.2011.02629.x.

Kioe-A-Sen, Nicole M. E., Manfred J. van Bergen, Theo E. Wong, and Salomon B. Kroonenberg. 2016. "Gold Deposits of Suriname: Geological Context, Production and Economic Significance." *Netherlands Journal of Geosciences - Geologie En Mijnbouw* 95 (4): 429–45. https://doi.org/10.1017/njg.2016.40.

Koltunov, Alexander, Susan L. Ustin, Gregory P. Asner, and Inez Fung. 2009. "Selective Logging Changes Forest Phenology in the Brazilian Amazon: Evidence from MODIS Image Time Series Analysis." *Remote Sensing of Environment* 113 (11): 2431–40. https://doi.org/10.1016/j.rse.2009.07.005.

Kumi, Samuel, Patrick Addo-Fordjour, Bernard Fei-Baffoe, Ebenezer J.D. Belford, and Yaw Ameyaw. 2021. "Land Use Land Cover Dynamics and Fragmentation-Induced Changes in Woody Plant Community Structure in a Mining Landscape, Ghana." *Trees, Forests and People* 4 (June): 100070. https://doi.org/10.1016/j.tfp.2021.100070.

Laurance, William F., José L. C. Camargo, Philip M. Fearnside, Thomas E. Lovejoy, G. Bruce Williamson, Rita C. G. Mesquita, Christoph F. J. Meyer, Paulo E. D. Bobrowiec, and Susan G.

W. Laurance. 2018. "An Amazonian Rainforest and Its Fragments as a Laboratory of Global Change." *Biological Reviews* 93 (1): 223–47. https://doi.org/10.1111/brv.12343.

Le Tourneau, François-Michel. 2016. "Is Brazil Now in Control of Deforestation in the Amazon?" *Cybergeo : European Journal of Geography*, January. https://doi.org/10.4000/cybergeo.27484.

Lobo, Felipe de Lucia, Pedro Walfir M. Souza-Filho, Evlyn Márcia Leão de Moraes Novo, Felipe Menino Carlos, and Claudio Clemente Faria Barbosa. 2018. "Mapping Mining Areas in the Brazilian Amazon Using MSI/Sentinel-2 Imagery (2017)." *Remote Sensing* 10 (8): 1178. https://doi.org/10.3390/rs10081178.

Lopez-Quintero, Carlos A., Gerben Straatsma, A. Esperanza Franco-Molano, and Teun Boekhout. 2012. "Macrofungal Diversity in Colombian Amazon Forests Varies with Regions and Regimes of Disturbance." *Biodiversity and Conservation* 21 (9): 2221–43. https://doi.org/10.1007/s10531-012-0280-8.

Malaviya, Sumedha, Madhushree Munsi, Gracy Oinam, and Pawan Kumar Joshi. 2010. "Landscape Approach for Quantifying Land Use Land Cover Change (1972–2006) and Habitat Diversity in a Mining Area in Central India (Bokaro, Jharkhand)." *Environmental Monitoring and Assessment* 170 (1–4): 215–29. https://doi.org/10.1007/s10661-009-1227-8.

Malm, Olaf. 1998. "Gold Mining as a Source of Mercury Exposure in the Brazilian Amazon." *Environmental Research* 77 (2): 73–78. https://doi.org/10.1006/enrs.1998.3828.

Manoli, Gabriele, Valeriy Y. Ivanov, and Simone Fatichi. 2018. "Dry-Season Greening and Water Stress in Amazonia: The Role of Modeling Leaf Phenology." *Journal of Geophysical Research: Biogeosciences* 123 (6): 1909–26. https://doi.org/10.1029/2017JG004282.

Miller, Ryan. 2019. "Revealed: Most Forested Countries In The World." *CEOWORLD Magazine* (blog). September 10, 2019. https://ceoworld.biz/2019/09/10/revealed-most-forested-countries-in-the-world/.

Mitraka, Zina, Fabio Del Frate, and Francesco Carbone. 2016. "Nonlinear Spectral Unmixing of Landsat Imagery for Urban Surface Cover Mapping." *IEEE Journal of Selected Topics in Applied Earth Observations and Remote Sensing* 9 (7): 3340–50. https://doi.org/10.1109/JSTARS.2016.2522181.

Moreau, Ines, and Pierre Defourny. 2012. "The Vegetation Phenology Detection in Amazon Tropical Evergreen Forests Using SPOT-VEGETATION 11-y Time Series." In *2012 IEEE International Geoscience and Remote Sensing Symposium*, 40–43. Munich, Germany: IEEE. https://doi.org/10.1109/IGARSS.2012.6351641.

Moreno-Sanchez, R. 2009. "Fragmentation of the Temperate and Tropical Forests in Mexico: Implications for Their Conservation and Sustainable Management." In , 511–17. Cyprus. https://doi.org/10.2495/SDP090472.

NASA Earth Observatory. 2011. "2010 Drought in the Amazon Forest." Text.Article. NASA Earth Observatory. April 16, 2011. https://earthobservatory.nasa.gov/images/50136/2010-drought-in-the-amazon-forest.

Nicolau, Andrea Puzzi, Kelsey Herndon, Africa Flores-Anderson, and Robert Griffin. 2019. "A Spatial Pattern Analysis of Forest Loss in the Madre de Dios Region, Peru." *Environmental Research Letters* 14 (12): 124045. https://doi.org/10.1088/1748-9326/ab57c3.

Park, Chris C. 2002. *Tropical Rainforests*. Routledge.

Perez, Gustavo J. 1970. "The Mexican Mining Concession-Its Features, Regulation and Practice Seminar on the Law of Real Property Acquisition in Mexico." *Arizona Law Review* 12 (2): 356–73.

Peterson, Garry D., and Marieke Heemskerk. 2001. "Deforestation and Forest Regeneration Following Small-Scale Gold Mining in the Amazon: The Case of Suriname." *Environmental Conservation* 28 (2): 117–26. https://doi.org/10.1017/S0376892901000121.

Pinage, Ekena Rangel, David M. Bell, Matthew Gregory, Ngoc Nguyen Tran, Wenjie Zhang, and Alfredo Huete. 2020. "Effects of Tropical Forest Degradation on Amazon Forest Phenology." In *IGARSS 2020 - 2020 IEEE International Geoscience and Remote Sensing Symposium*, 4516–19. Waikoloa, HI, USA: IEEE. https://doi.org/10.1109/IGARSS39084.2020.9324161.

Pinheiro, M.C.N., M.E. Crespo-López, J.L.F. Vieira, T. Oikawa, G.A. Guimarães, C.C. Araújo, W.W. Amoras, et al.. 2007. "Mercury Pollution and Childhood in Amazon Riverside Villages." *Environment International* 33 (1): 56–61. https://doi.org/10.1016/j.envint.2006.06.024.

Rahm, M, B Julian, A Lauger, R De Carvalho, L Vale, J Totaram, K.A Cort, et al.. "Monitoring the Impact of Gold Mining on the Forest Cover and Freshwater in the Guyana Shield ," 2015.

Ratana, P., A. Huete, and K. Didan. 2006. "MODIS EVIbased Variability in Amazon Phenology across the Rainforest-Cerrado Ecotone." In *2006 IEEE International Symposium on Geoscience and Remote Sensing*, 1942–44. Denver, CO, USA: IEEE. https://doi.org/10.1109/IGARSS.2006.502.

Riitters, Kurt H., James D. Wickham, Robert V. O'Neill, K. Bruce Jones, Elizabeth R. Smith, John W. Coulston, Timothy G. Wade, and Jonathan H. Smith. 2002. "Fragmentation of Continental United States Forests." *Ecosystems* 5 (8): 815–22. https://doi.org/10.1007/s10021-002-0209-2.

Riitters, Kurt, James D. Wickham, Robert O'Neill, K. Bruce Jones, and Elizabeth Smith. 2000. "Global-Scale Patterns of Forest Fragmentation." *Conservation Ecology* 4 (2): art3. https://doi.org/10.5751/ES-00209-040203.

Roch, Laura, and Jochen A. G. Jaeger. 2014. "Monitoring an Ecosystem at Risk: What Is the Degree of Grassland Fragmentation in the Canadian Prairies?" *Environmental Monitoring and Assessment* 186 (4): 2505–34. https://doi.org/10.1007/s10661-013-3557-9.

Rodrigues, Eliana. 2006. "Plants and Animals Utilized as Medicines in the Jaú National Park (JNP), Brazilian Amazon." *Phytotherapy Research* 20 (5): 378–91. https://doi.org/10.1002/ptr.1866.

Sánchez-Cuervo, Ana María, Letícia Santos de Lima, Francisco Dallmeier, Paola Garate, Adriana Bravo, and Hadrien Vanthomme. 2020. "Twenty Years of Land Cover Change in the Southeastern Peruvian Amazon: Implications for Biodiversity Conservation." *Regional Environmental Change* 20 (1): 8. https://doi.org/10.1007/s10113-020-01603-y.

Siqueira-Gay, Juliana, Laura J. Sonter, and Luis E. Sánchez. 2020. "Exploring Potential Impacts of Mining on Forest Loss and Fragmentation within a Biodiverse Region of Brazil's Northeastern Amazon." *Resources Policy* 67 (August): 101662. https://doi.org/10.1016/j.resourpol.2020.101662.

Soares-Filho, Britaldo, Paulo Moutinho, Daniel Nepstad, Anthony Anderson, Hermann Rodrigues, Ricardo Garcia, Laura Dietzsch, et al.. 2010. "Role of Brazilian Amazon Protected Areas in

Climate Change Mitigation." *Proceedings of the National Academy of Sciences of the United States of America* 107 (24): 10821–26. https://doi.org/10.1073/pnas.0913048107.

Sonter, Laura J., Diego Herrera, Damian J. Barrett, Gillian L. Galford, Chris J. Moran, and Britaldo S. Soares-Filho. 2017. "Mining Drives Extensive Deforestation in the Brazilian Amazon." *Nature Communications* 8 (1): 1013. https://doi.org/10.1038/s41467-017-00557-w.

Swenson, Jennifer J., Catherine E. Carter, Jean-Christophe Domec, and Cesar I. Delgado. 2011. "Gold Mining in the Peruvian Amazon: Global Prices, Deforestation, and Mercury Imports." Edited by Guy J-P. Schumann. *PLoS ONE* 6 (4): e18875. https://doi.org/10.1371/journal.pone.0018875.

T V, Ramachandra, Bharath Setturu, and Subash Chandran. 2016. "Geospatial Analysis of Forest Fragmentation in Uttara Kannada District, India." *Forest Ecosystems* 3 (1): 10. https://doi.org/10.1186/s40663-016-0069-4.

Velásquez Ramírez, Manuel Gabriel, Juan Antonio Guerrero Barrantes, Evert Thomas, Luis Alfredo Gamarra Miranda, Martin Pillaca, Lily Denise Tello Peramas, and Luis Rubén Bazán Tapia. 2020. "Heavy Metals in Alluvial Gold Mine Spoils in the Peruvian Amazon." *CATENA* 189 (June): 104454. https://doi.org/10.1016/j.catena.2020.104454.

Wulder, Michael A., Joanne C. White, and Nicholas C. Coops. 2011. "Fragmentation Regimes of Canada's Forests: Fragmentation Regimes of Canada's Forests." *The Canadian Geographer / Le Géographe Canadien* 55 (3): 288–300. https://doi.org/10.1111/j.1541-0064.2010.00335.x.

A. APPENDIX

GEE SCRIPT

Step 1:

```
//1. IMPORT, FILTER AND DISPLAY LANDSAT IMAGES

//import image collection
var L8 = ee.ImageCollection('LANDSAT/LC08/C02/T1_L2')

//Reduce Landsat 8 collection by region, date, and cloud cover
var Raw_images_2016 = L8.filterBounds(region)
                        .filterDate('2019-01-01', '2020-01-01')
                        .filter(ee.Filter.lte('CLOUD_COVER',6));
print(Raw_images_2016);

//Display Map
Map.addLayer(Raw_images_2016);
Map.centerObject(region, 9);
```

Step 2:

```
//2. CREATE IMAGE COLLECTION FROM FINAL IMAGES

// Select the final 4 images.
var upperleft = ee.Image('LANDSAT/LC08/C02/T1_L2/LC08_229056_20191010');
var upperright = ee.Image('LANDSAT/LC08/C02/T1_L2/LC08_228056_20190901');
var lowerleft = ee.Image('LANDSAT/LC08/C02/T1_L2/LC08_229057_20190908');
var lowerright = ee.Image('LANDSAT/LC08/C02/T1_L2/LC08_228057_20200919');


// Create one collection of the final 4 images.
var Final_images_2016 = ee.ImageCollection([upperleft, upperright, lowerleft, lowerright]);
print('Final Image Collection: ', Final_images_2016);


Map.addLayer(Final_images_2016, {bands: ['SR_B4', 'SR_B3', 'SR_B2'], min: 3000, max: 24000}, 'Final Images 2016');
```

Step 3:

```
//3. SCALE BANDS FOR VIZUALISATION USING CLOUD MASK FUNCTION
//Create function to mask clouds for L8 surface reflectance data
function L8_cloud_mask(image) {
  // Bit 0 - Fill
  // Bit 1 - Dilated Cloud
  // Bit 2 - Cirrus
  // Bit 3 - Cloud
  // Bit 4 - Cloud Shadow
  var qaMask = image.select('QA_PIXEL').bitwiseAnd(parseInt('00000', 2)).eq(0);
  var saturationMask = image.select('QA_RADSAT').eq(0);

  // Apply the scaling factors to the appropriate bands.
  var opticalBands = image.select('SR_B.').multiply(0.0000275).add(-0.2);
  var thermalBands = image.select('ST_B.*').multiply(0.00341802).add(149.0);

  // Replace the original bands with the scaled ones and apply the masks.
  return image.addBands(opticalBands, null, true)
      .addBands(thermalBands, null, true)
      .updateMask(qaMask)
      //.updateMask(saturationMask);
}


//Apply the mask to the final image collection
var Masked_Final_Images_2016 = ee.ImageCollection([upperleft, upperright, lowerleft, lowerright])
                          .map(L8_cloud_mask);

Map.addLayer(Masked_Final_Images_2016, {bands: ['SR_B4', 'SR_B3', 'SR_B2'], min: 0, max: 0.3}, 'Masked Final Images


var upperrightmasked = upperright.select('SR_B1', 'SR_B2', 'SR_B3', 'SR_B4', 'SR_B5', 'SR_B6', 'SR_B7')
```

Step 4:

```
//4. UNSUPERVISED CLASSIFICATION
// Display the sample region.

Map.addLayer(ee.Image().paint(trainingunsup, 0, 2), {}, 'trainingunsupervised');

// Make the training dataset.
var training = ee.Image(upperrightmasked.sample({
  region: trainingunsup,
  scale: 30,
  numPixels: 5000
}));

// Instantiate the clusterer and train it.
var clusterer = ee.Clusterer.wekaKMeans(10).train(training);

// Cluster the input using the trained clusterer.
var result = upperrightmasked.cluster(clusterer);

// Display the clusters with random colors.
Map.addLayer(result.randomVisualizer(), {}, 'unsupervisedclassification');

//Map.addLayer(qaMask,{});
//print('QA_mask',qaMask);
```

Step 5:

```
//5. CREATE AND EXPORT CLOUD MASK ON INDIVIDUAL IMAGE
var qaMask2 = upperright.select('QA_PIXEL').bitwiseAnd(parseInt('11000', 2)).eq(0);
Map.addLayer(qaMask2);
```

Step 6:

```
//6. SUPERVISED CLASSIFICATION - CART

// set the selection bands
var predictionBands = ['SR_B1', 'SR_B2', 'SR_B3', 'SR_B4', 'SR_B5', 'SR_B6', 'SR_B7'];
//print (predictionBands);

// Training phase
var trainingData = water.merge(mines).merge(forest).merge(urban).merge(agriculture)

//var label = 'Landcover';

// sample the regions
var classifierTraining = upperrightmasked.select(predictionBands).sampleRegions(
                  {collection: trainingData,
                   properties: ['LC'],
                   scale: 30 });

//train the classifier
var classifier =  ee.Classifier.smileCart().train({features:classifierTraining,
                                        classProperty: 'LC',
                                        inputProperties: predictionBands});

// get the classified image
var classified = upperright.select(predictionBands).classify(classifier);

// Assigning palette
var Palette = [
  'f7e084', // mines
  'aec3d4', //  Water
  '369b47', // forest
  'cb162e', //urban
  'df52e3', //agriculture
 ];

//add the classified image to the map
Map.addLayer(classified,  {min: 1, max: 5, palette: Palette}, "CART Upper Right");
```

Step 7:

```
//7. VALIDATION

// IMPORT, FILTER AND DISPLAY SENTINEL IMAGES + COLLECT VALIDATION POINTS

//import image collection
var S2 = ee.ImageCollection('COPERNICUS/S2')

//Reduce Sentinel collection by region, date, and cloud cover
var S2raw_images_2016 = S2.filterBounds(region2)
                          .filterDate('2019-01-01', '2020-01-01')
                          .filter(ee.Filter.lt('CLOUDY_PIXEL_PERCENTAGE', 2));
print(S2raw_images_2016);

var image = ee.Image(S2raw_images_2016.mosaic());



//Display Map
Map.addLayer(image, {min:0,max:4500,bands:"B4,B3,B2"}, "Sentinel");
Map.centerObject(region, 9);
```